TECHNISCHE
UNIVERSITÄT
WIEN
Vienna University of Technology

AUTOMATION & CONTROL INSTITUTE
INSTITUT FÜR AUTOMATISIERUNGS-
& REGELUNGSTECHNIK

# Automated Probe-Sample Alignment for the Evaluation of Integrated Circuits

## DIPLOMARBEIT

Ausgeführt zum Zwecke der Erlangung des akademischen Grades eines
Diplom-Ingenieurs (Dipl.-Ing.)

unter der Leitung von

Univ.-Prof. Dr.sc.techn. Georg Schitter
Dipl.-Ing. Mathias Poik

eingereicht an der

Technischen Universität Wien
Fakultät für Elektrotechnik und Informationstechnik
Institut für Automatisierungs- und Regelungstechnik

von

Thomas Hackl, BSc
Matrikelnummer: 01328859

Wien, im 01 2020

**Advanced Mechatronic Systems Group**
Gußhausstraße 27-29, A-1040 Wien, Internet: http://www.acin.tuwien.ac.at

# Acknowledgement

This diploma thesis was conducted during my master's program at the Automation and Control Institute of the Technical University Vienna.

Hereby I would like to thank all the people who supported me in the realization of this work.
First of all, special thanks to my daily supervisor Dipl.-Ing. Mathias Poik, who tirelessly helped me with his advice and profound knowledge throughout the whole thesis. I also want to thank Univ.-Prof. Dr.sc.tech. Georg Schitter for the opportunity and making this work possible. Thanks to his team (Advanced Mechatronics Systems group) for having such a great work environment and ease of communication.
Special thanks to all my friends and colleagues at the university, that i got to know and appreciate. In particular, thanks to Dipl.-Ing. Florian Krimmel, who proofread my thesis and for the fruitful discussions during my whole studies.

Finally and most importantly, i would like to express my deepest gratitude to my whole family, especially my parents Aloisia and Friedrich, my brother Christoph, my sister Andrea, her husband Josef and their daughter Annika. You enabled everything and supported me during my entire life.

Thank you.

# Abstract

By measuring and testing integrated circuits, quality and functionality can already be determined during and after the production. But with ever increasing demands, such as cost or efficiency, the complexity and density of the circuits is also increasing. This leads to ever smaller structures and contact pads, that pose challenges to the measurements. As a result, a more accurate alignment between the measurement probe to the investigated circuit is necessary. Currently, testing is achieved utilizing manual probing stations, where the alignment is usually done by a human. Due to bad reproducibility and slow execution, automation of this process is proposed in this work. To this end, a vision guided alignment system is implemented and its accuracy is evaluated.

Various machine-vision techniques for spatial detection of the objects position, such as the probes tip and the samples contact pad, are implemented and compared. The images are acquired utilizing a camera and an objective lens. To measure the vertical positions, the focus of this optical system is adjusted with the usage of focusing algorithms. The method "Tenenbaum variance" shows the best performance. The horizontal position of the objects is measured using "Template matching". After the measurement of the spatial positions, alignment is achieved by controlling positioning stages. Algorithms to accelerate the alignment process, as well as methods to increase the robustness are presented and compared.

Since the determination of the positioning accuracy with usual probes is not possible, an atomic force microscope utilizing a piezoresistive cantilever is implemented. This offers the possibility of performing a scan after the completed alignment, thereby determining the spatial offset. The achieved positioning accuracy in vertical and horizontal direction are 880 nm and 490 nm, respectively. The average duration for the alignment process is 48 s. Limits, such as the objective lenses depth of field and magnification as well as the cameras resolution, result from a trade-off between accuracy, execution speed and ease of implementation.

# Zusammenfassung

Durch das Messen und Testen von integrierten Schaltkreisen, kann bereits während und nach der Produktion die Qualität und Funktionalität bestimmt werden. Mit steigenden Anforderungen an Kosten oder Effizienz steigt jedoch auch die Komplexität und Dichte der Schaltungen. Dies führt zu immer kleiner werdenden Strukturen und Kontaktflächen, die Herasuforderungen an die Messungen stellen. Infolgedessen ist eine genauere Ausrichtung zwischen der Spitze der Messprobe und dem zu untersuchenden Schaltkreis erforderlich. Aktuell werden Messungen mit manuellen Prüfstationen durchgeführt, bei denen die Ausrichtung von einem Menschen vorgenommen wird. Aufgrund der schlechten Reproduzierbarkeit und langsamen Ausführung wird in dieser Arbeit eine Automatisierung dieses Prozesses vorgeschlagen. Zu diesem Zweck wird eine kamerabasierte Regelung implementiert und dessen Genauigkeit bewertet.

Verschiedene Bildverarbeitungstechniken zur räumlichen Erfassung der Objektpositionen, wie der Spitze der Messprobe sowie der Kontaktfläche des Schalkreises, sind implementiert. Die Bilder werden mit einer Kamera und einem Objektiv aufgenommen. Um die vertikalen Positionen zu ermitteln, wird der Fokus dieses optischen Systems unter der Verwendung von Fokussierungsalgorithmen angepasst. Die Methode "Tenenbaum Varianz" liefert hierbei die besten Ergebnisse. Die horizontale Position der Objekte wird mit der Methode "Template matching" gemessen. Nach dem Erfassen der Positionen, werden die Komponenten mittels Linearmotoren zueinander ausgerichtet. Algorithmen zur Beschleunigung des Ausrichtungsprozesses sowie Methoden zur Erhöhung der Robustheit werden vorgestellt und verglichen.

Da die Bestimmung der Positioniergenauigkeit mit üblichen Messproben nicht möglich ist, wird ein Rasterkraftmikroskop mit einem piezoresistiven Cantilever implementiert. Dies bietet die Möglichkeit, nach erfolgter Ausrichtung einen Scan durchzuführen, um so den räumlichen Versatz zu ermitteln. Die erreichte Positioniergenauigkeit in vertikaler und horizontaler Richtung beträgt 880 nm bzw. 490 nm. Die durchschnittliche Dauer für den Ausrichtungsprozess beträgt 48 s. Limiten, wie die Tiefenschärfe und die Vergößerung des Objektivs sowie die Kameraauflösung, ergeben sich aus einem Kompromiss zwischen Genauigkeit und Geschwindigkeit.

# Contents

# List of Figures

# List of Tables

# Acronyms

| | |
|---|---|
| AFM | atomic force microscopy |
| CoC | circle of confusion |
| DAQ | data acquisition |
| DOF | depth of field |
| DUT | device under test |
| FOV | field of view |
| FPS | frames per second |
| FWHM | full width at half maximum |
| HEMT | high electron mobility field-effect transistor |
| IC | integrated circuit |
| KPFM | kelvin probe force microscopy |
| LNA | low-noise amplifier |
| LRM | line-reflect-match |
| MEMS | micro-electromechanical systems |
| MFM | magnetic force microscopy |
| NA | numerical aperture |
| ROI | region of interest |
| RWPS | real world pixel size |
| SEM | scanning electron microscope |
| SOLT | short-open-load-thru |
| TMIC | THz monolithic integrated circuit |
| TRL | thru-reflect-line |
| VNA | vector network analyzer |

# CHAPTER 1

# Introduction

Every electronic circuit needs to be tested in order to prove its functionality. This is achieved by connecting a measuring device to the investigated circuit. Contacting electronic circuits by measurement probes, is challenging due to their small dimensions. In this work a vision-guided approach for for automated probe-circuit alignment is developed.

## 1.1 Motivation

*Complexity of integrated circuits has approximately doubled every year since their introduction. Cost per function has decreased several thousandfold, while system performance and reliability have been improved dramatically.*

- Gordon E. Moore [1]

This statement, commonly referred to as Moores' law, exists for more than 50 years now and remained true till today [2]. Driving forces behind the semiconductor industry have led to a significant increase in the development of new manufacturing technologies [3]. Reduced cost per chip, raised functionality with the embedding of sensor elements on chip or increase of speed were, among others, the main drivers [4]. With this development, the semiconductor industry could maintain its performance increase for the next years. This rapid progress will lead to significant challenges in verification and testing of integrated circuits (ICs) [5]. These steps are essential to maintain the required reliability of such systems. However, with the ever increasing packing density and the decrease of structure sizes down to the nanometer level, the size of contact pads is shrinking as well. Additionally, a trend towards higher frequencies can be recognized [6]. This is a result of the ever growing demand for faster and more reliable communication technology. Development of THz monolithic integrated circuits

(TMICs) led to the integration of higher frequencies (up to 1 THz) on chips [7]. The corresponding smaller wave-length results in the need for smaller electronic connections, thus driving the packing density even further. This makes the contacting of these pads, which are usual in the range of several tens of $\mu m^2$ a real challenge. The development of verification and testing systems is therefore an essential step to further advance the development of semiconductor components.
Contacting and testing of ICs is currently done via special probing stations [8]. Figure 1.1 shows a schematic of such a system. The investigated chip, further referred to as sample, is held in place using a vacuum pump. With a look through the microscope or camera, the operator then adjusts the position of the probing arms, in order to move them to the samples contact pads or waveguides. This is done via precision screws or positioning stages. Via direct or indirect contact (capacitive/inductive coupling), signals are then fed through the probe tip to the sample. These signals are generated by measurement devices, such as vector network analyzers (VNAs) or other signal sources. By measuring the response of the sample, the functionality is verified.

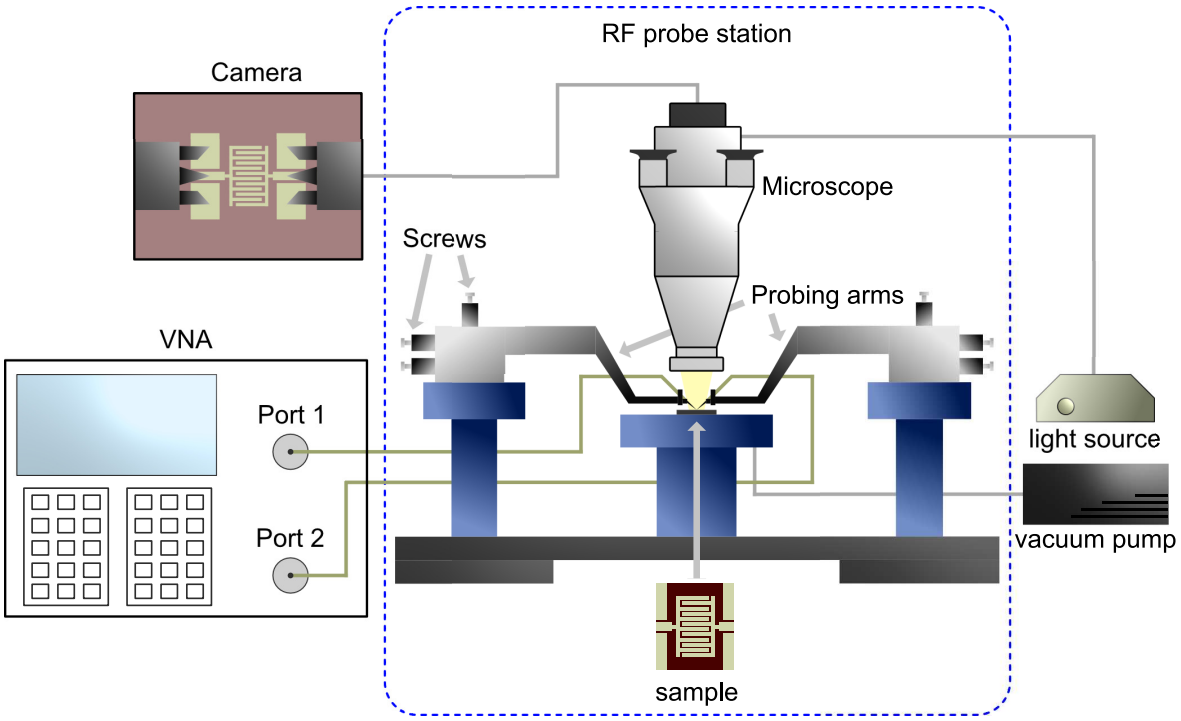


Figure 1.1: Schematic of a probe station.

However, a proper alignment between the probe tips and the contact pads is necessary to gain meaningful measurement results [9]. Unintended rotations or positioning offsets of the probe can cause different contact conditions, which lead to unknown contact impedances. Spurious signal reflections, attenuations or coupling to adjacent circuits may be the result. Figure 1.2 shows an example of a correct (top) and rotated (bottom) probe/sample alignment. The unintended rotation of the manually aligned probe results in an unknown contact impedance and therefore inaccurate measurement results [10].

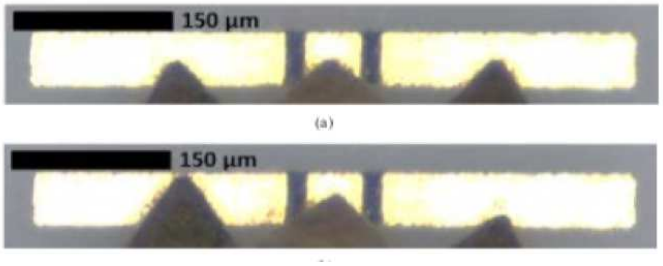


Figure 1.2: Probe misalignment [9].

Slow operation, vibrations of the hand and the physical state of the human operator are limiting factors on the achievable alignment accuracy. Furthermore the individual operator's skills which are based on their experience may provide different contact conditions of the probe as it is depending on the manual observation of the tip. In this work automation of the alignment process is proposed to increase the accuracy and reliability of probing systems. Vision-guided systems offer themselves as they are easy to set up and can act as an upgrade to existing systems. A faster and more accurate alignment procedure is the consequence [11].

## 1.2 Aim of the Thesis

Motivated by above mentioned statements to automate the probe/sample alignment in probing stations, the objective of this master thesis is to design and build a setup, where a probe is accurately aligned to a sample utilizing a vision-guided approach. By visually measuring the horizontal and vertical position of the probes tip and the samples contact pad, a positioning error is determined and minimized. Following from the visual approach, the system should be able to operate without the need for accurate calibration between the stages and the camera itself. Alignment precision in the micrometer range is targeted as the size of contact pads is usually in the range of several tens of $\mu m^2$. To determine the alignment accuracy, a separate setup needs to be integrated, as it can't be evaluated with the visual-guided system itself. The evaluation precision should be at least an order of magnitude higher. Based on the components and the used algorithms, parameters should be identified, which have a limiting effect on the alignment accuracy. Concluding above words, following steps define the goal of this thesis:

- Design and implementation of a vision-guided probe/sample alignment system
- Development of a system which evaluates the positioning accuracy
- Derivation of limiting factors of the alignment system

## 1.3 Outline

The following thesis is organized as follows. Chapter 2 presents the state of the art of probing stations and related research topics, regarding automation and developments towards higher frequencies. Further, an overview of current vision-guided control approaches will be introduced. In Chapter 3, the proposed system is presented and general procedures used to achieve the goal are depicted. Chapter 4 gives an overview on the theory of the used machine-vision techniques. Methods to determine optimal focus and the lateral position of an object are discussed. The implementation, consisting of the alignment- and the evaluation-system components can be found in Chapter 5. The carried out measurement procedures and results are presented in Chapter 6. This work ends with a conclusion and an outlook in Chapter 7.

# CHAPTER 2

# State of the Art

This chapter presents the basic principle of manual and semi-automatic probe stations. Several fields of research dealing with the probe/sample alignment will be presented. At the end of the chapter an insight into several vision-guided approaches used in other scientific fields will be given.

## 2.1 Probe Stations

Contacting and testing of ICs is usually carried out utilizing probing stations [12]. Yet, they can be separated into two areas. On one side, industrial in-line testing has to be fast and easily scalable, as the time-to-market needs to be as low as possible. Semi-automatic probing stations were developed to automatically exchange the investigated samples and therefore increase the speed of such systems. Additionally, there are usually large quantities of chips in the industry. Therefore, the expensive development of automated measurement routines is economically feasible as they can easily scale. On the other side, for research and prototype purposes, such expenses are not economic, as the number of samples is usually low. Therefore, manual probing stations are used. The advantage of manually operated stations is the flexibility. However, the drawback is the inaccuracy of the manual alignment process itself.

### 2.1.1 Semi-Automatic Probe Stations

Semi-automatic probe stations, as depicted in Figure 2.1(a) (TS3000, MPI Corporation, Taiwan), are capable of automatically exchanging the investigated sample. They are designed to be added into the production line. After a new wafer gets loaded, cameras are used to detect its orientation using integrated reference points on the wafer. Via preprogrammed measurement steps, probes are sequentially placed onto individual

dies of the wafer and test signals are applied. After checking each die, the wafer gets unloaded and fed to the next production step. Figure 2.1(b) shows a detailed view at the semi-automatic probing station.

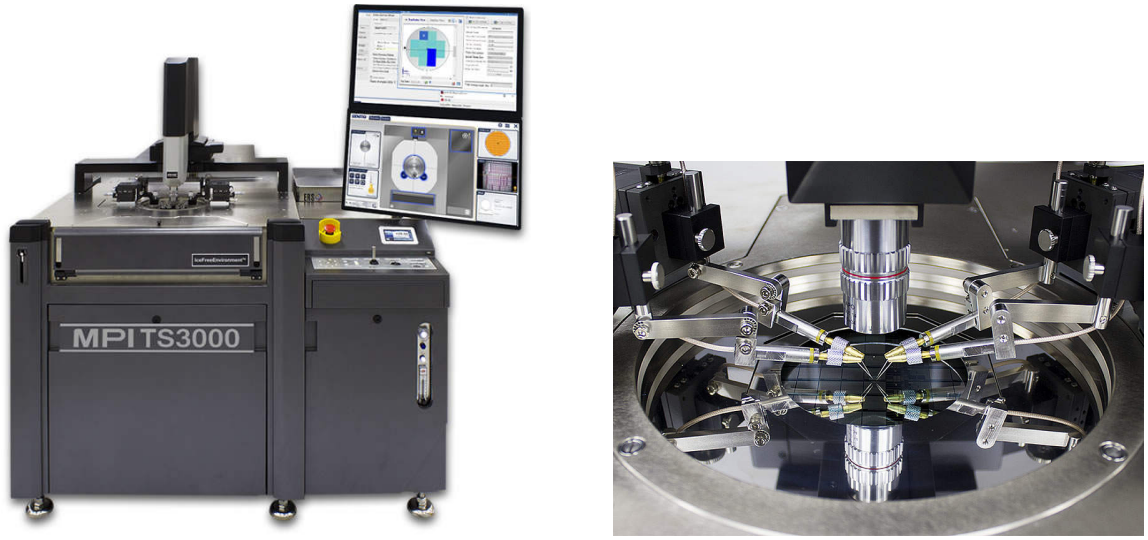


Figure 2.1: (a) Commercially available semi-automatic probe station / (b) a detailed view on the alignment setup [13].

The term 'semi-automatic' refers to the fact that manual steps are still required. For instance, the initialization of the probe-tips position. The machine needs to know the position of the probe in relation to the wafer at every process step. Via teaching the station an initial position of the probe, it adapts its programmed steps with this offset. In industrial applications it makes sense to afford complex programmed measurement routines, due to the huge number of chips. The ease of scalability makes it economical. In contrast to that, research purposes or prototype development is usually related to small amounts of samples. Manual probe stations help meeting the requirements of flexibility given here.

### 2.1.2 Manual Probe Stations

Figure 2.2 shows a commercially available manual probe station (MPS150, FormFactor, USA), with a detailed view on the sample. The flexibility of this system derives from the four freely movable probing arms. Each of them is magnetically attached to the base plate. Alignment is achieved by turning the screws at each probing arm.

Figure 2.2: Commercially available manual probe station with a detailed view of the probes/sample through the microscope [14, 15].

The physical condition and the vibrations of the hand from the operator cause the need for large contact pads (several tens of $\mu m^2$), like the ones in the lower left image of Figure 2.2. In the next section, different approaches to improve the measurement accuracy are discussed.

### 2.1.3 Research Topics

To meet the growing demands of probing stations, research focuses on several fields, in order to improve the quality and reliability of measurements. Besides the development of newer probes, which are capable of measuring up to higher frequencies, automation of the alignment process is a big step to fulfill the requirements. Approaches for contactless measurements are also getting more into the spotlight as they are non-invasive.

#### Contactless Measurement

Conventional testing of ICs is done by placing the probe directly onto the contact pad. The result can be unwanted contact point deformation and the need for regular probe cleaning or replacement. Accumulated debris can also cause negative effects on the measurement [16]. This led to the development of non-invasive contactless testing techniques [17] . Via inductively or capacitively coupled antennas, the power supply and test signals are coupled into and out of the investigated circuit [18]. Minor misalignments between the probe and the antenna of the device under test (DUT) can be tolerated. However, crosstalk to adjacent circuits and channel interference is getting

an issue as the pad density grows [19]. Additionally, the coupling capacitance and inductance between the two antennas limits the transmission gain. Rather large ($80\mu m$ x $80\mu m$) contact pads are a requirement for the system to work. Figure 2.3 shows an example sketch of a contactless measurement.

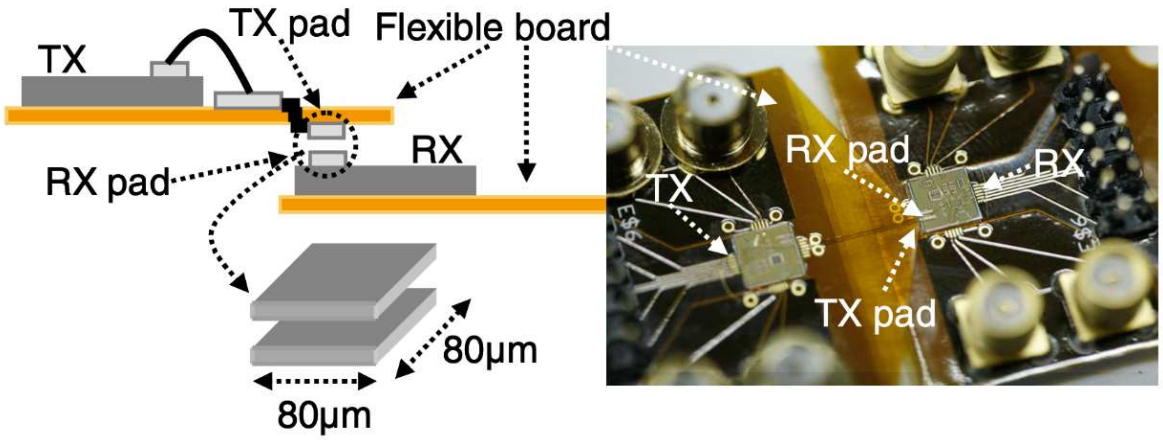


Figure 2.3: Contactless measurement [20].

Additionally, such techniques are currently only applicable to frequencies up to several GHz. Measurements with higher frequencies are still depending on the development of probes and more accurate alignment techniques.

### Development of Probes

Sub-millimeter or THz systems are usually based on rectangular waveguides or optics, which are bulky and difficult to integrate. Due to the advances in the development of TMICs, this frequency range becomes more and more available [21]. Improvement of measurement systems at these frequencies would aid further developments. However, the associated smaller dimensions of the contact pads and planar waveguides are becoming a real issue as they need to be contacted. This task is usually done by probes. They are the core of the measurement systems as they feed the test signals in and out of the investigated circuits. While maintaining a low DC contact resistance, they should provide low insertion and return loss of the high frequency test signals. Current research regarding the development of probes, which are capable of performing measurements up to 1 THz can be found in [22, 23]. Figure 2.4(a) and 2.4(b) show a sketch and a real world implementation of a sub-millimeter wavelength probe, respectively.

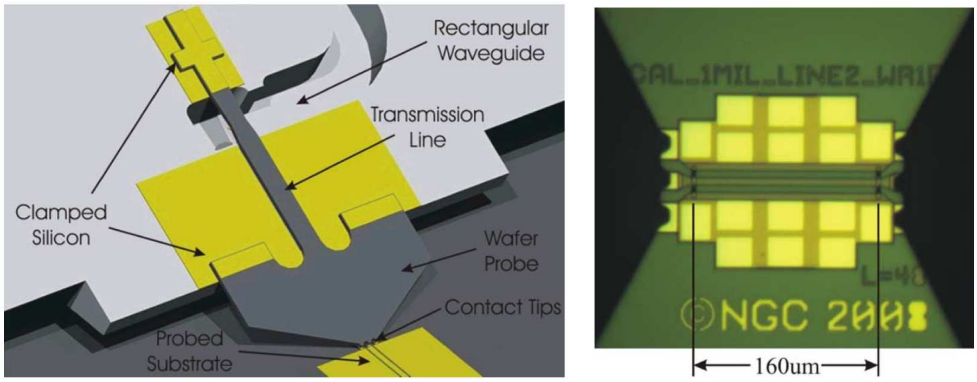


(a) (b)

Figure 2.4: THz Probe [24].

The use of smaller probes introduces the requirement of more accurate positioning techniques. Uncertainties in the position will result in variations of the probe performance [25]. Additionally, as the frequency increases the parasitic effects of the contact pad itself leads to uncertainties in the measurement.

### Measurement Calibration

When measuring high frequency systems, the influence of the measurement device itself and its feeding cables should be cancelled out [26]. The reference plane of a measurement is the point were the measurement is actually done. In the form of a VNA, this reference plane is at its ports. When cables are used, a calibration needs to be done in order to model their influence on the measurement. This model is then subtracted from the measurement results. This results in the shift of the reference plane to the end of the cables or to the probes tip. A method which describes this routine is short-open-load-thru (SOLT) [27]. However, the reference plane should be exactly at the border of the DUT, which is usually after the contact pads [28, 29]. Therefore, an equivalent circuit of the contact pads get modelled, which is then subtracted from the measurement. With increasing frequency, such models become extremely complex. Newer techniques, such as line-reflect-match (LRM) or thru-reflect-line (TRL), were developed to move the reference plane from the probes tip to the DUT, overcoming the influence of the contact pad [30]. This results in minimizing the measurement uncertainties.
The measurement reproducibility, however, is a combination of the measurement uncertainty and the contact repeatability. Therefore, reliable contacts are nowadays the key to achieve meaningful and reproducible data. To address this issue, automation was proposed to increase contact repeatability.

### Automation of the Alignment Process

One of the main issues in IC testing was proven to be the probe positioning repeatability throughout the measurement [26]. After an initial probe calibration process, the actual measurement is carried out. Probe position repeatability needs to be ensured for both

steps, to preserve measurement resolution. Small deviations in the micrometer range (XYZ - direction and Θ - rotation) can cause huge measurement errors, especially as the frequency is increased [31]. Replacing the precision screws with positioning stages and automation of the alignment was shown to be useful to detect and correct possible positioning errors [32, 9]. Figure 2.5 shows an automated probe to sample alignment process. The probe touches down on the sample at several chosen positions. By constantly measuring the signal response of the sample, the contact pad and the probe tips shape get mapped. After the mapping phase the correct positioning offset is determined and corrected.

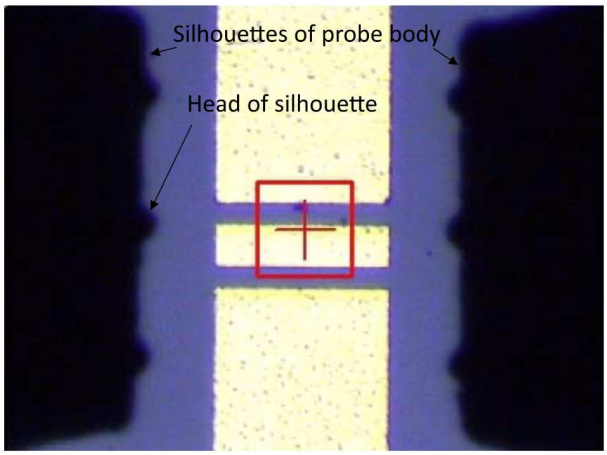


Figure 2.5: Automated alignment via contact mapping [33].

Yet this approach is very accurate, it is proposed to focus on acceleration of the alignment process. Long initialization and mapping phases make it impracticable.

### Cryogenic Probe Stations

The development of high electron mobility field-effect transistors (HEMTs) or high temperature (70 K) superconductors led to performance improvement of satellite links and other low temperature applications [34]. Low-noise amplifiers (LNAs), which consist of HEMTs, are operated at cryogenic temperatures in order to improve the signal to noise ratio. Besides the limiting factor of noise in some applications, measurements of these types of devices at cryogenic temperatures can aid to understand device physics even further. This led to the development of probing stations operating at low temperatures (below 20 K) [35]. Since the whole alignment system is encapsulated and cooled down, challenges regarding accessibility evolve [36]. Cameras and alignment stages in the cooling-chamber are used to remotely align the probe to the sample. Vision-guided control schemes can be used to upgrade such systems, yet making the alignment process faster.

## 2.2 Vision-Guided systems

The term vision-guided refers to a position control scheme, where the sensing part is done by a camera. With the use of machine vision techniques, objects are detected. This information is then used to control actuators, which manipulate them. Several scientific fields already implement visually guided systems, to increase the reliability and accuracy.

### 2.2.1 Biology

Manipulation of biological cells is becoming increasingly important. Studying the activities of molecules such as dyes, proteins or nucleic acids can lead to advancements of our understanding in cell biology. Similar to the testing of ICs, such tasks are usually performed by manual or semi-automatic stations, which encounter poor repeatability or success rate [37]. With the growing complexity of cellular processes, common tasks like injection, aspiration and gripping of cells is getting ever more time consuming. Especially when it comes to cell sorting [38]. High manipulation rates with optimal reproducibility are considered as a prerequisite for reliable bio-micromanipulation systems [39]. Many grippers were developed to aid the ease of manual manipulation [40, 41]. Parameters like thermal expansion, compact structure and ease of use were considered to make the usage as reproducible and accurate as possible. Figure 2.6 shows an example of a mechanical gripper manipulating a cyanobacteria cell.

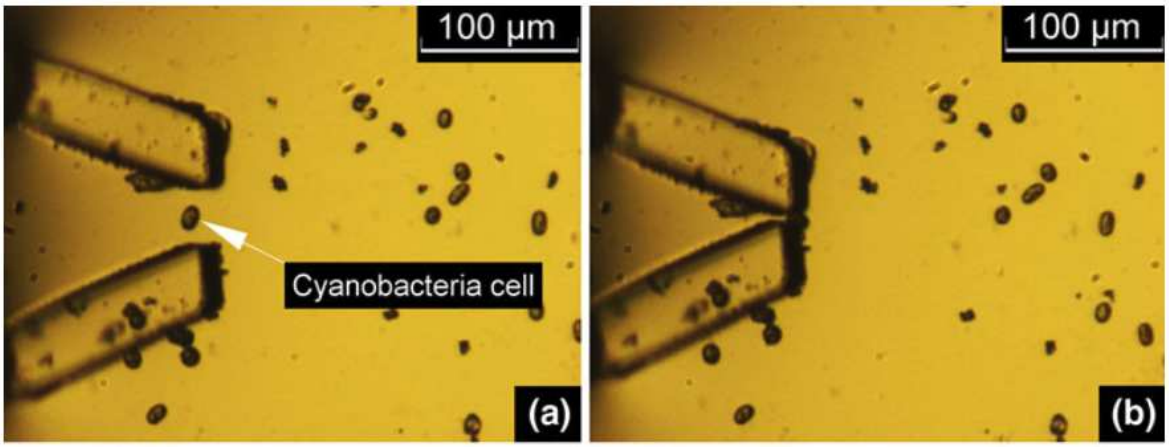


Figure 2.6: Mechanical gripper manipulating a cyanobacteria cell [42].

However, bottlenecks regarding quantitative bio-micromanipulation prevent further development. Automation was proposed to enable higher manipulation rates. Especially vision-guided automation, as it encounters versatile deployment and no complicated preparation or setup [43]. The advantage of fast and cheap digital imaging technology has allowed the implementation of easy to set up visual-guided systems.

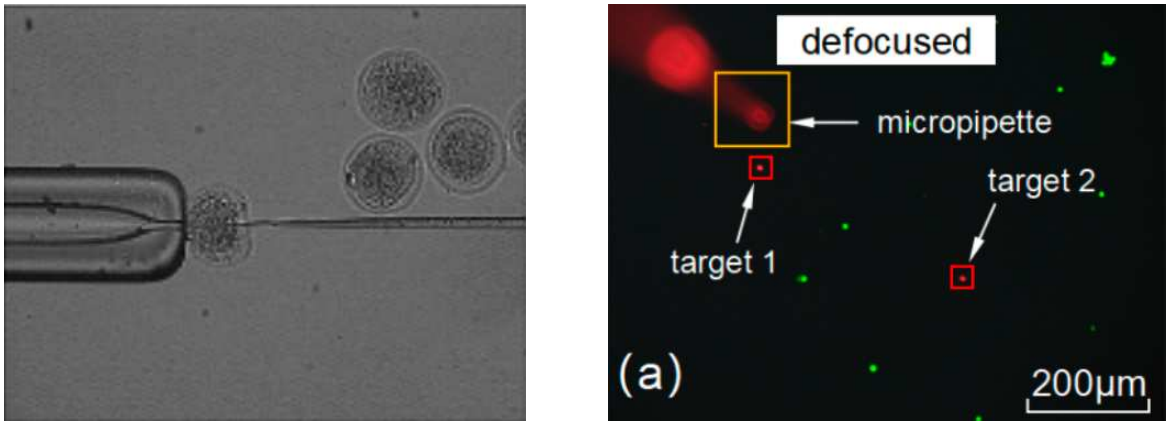


(a) (b)

Figure 2.7: (a) Manipulation of a biological cell using vision guided pipettes [39] / (b) Vision guided automated cell sorting [38].

Figure 2.7(a) shows an example of an automatic vision-guided cell manipulation. The cell is held in place via a suction pipette and manipulated with an injection pipette. Figure 2.7(b) visualizes the automated cell sorting process presented in [38]. It has been shown that vision guided automation has a positive contribution on the way how cell manipulation is performed. Kinematic model errors of the mechanism can be compensated due to the automated approach. High manipulation rates at good reproducibility were the result. Further, automatic transgenic operations can be realized. Future work in this direction will focus on accelerating the manipulation task while maintaining or even increasing the accuracy.

### 2.2.2 Micromechanics

Huge developments in the field of micro-electromechanical systems (MEMS) could be observed in the last years [44]. Yet, microassembly can overcome some inherent limitations of conventional MEMS devices [45]. As the fabrication is limited to planar or 2.5D shapes, microassembly can aid the manufacturing of complex spatial mechanisms. Additionaly, it can be used to assemble components, fabricated with different micromachining processes, that would otherwise be incompatible. Via manipulators, several planar machined parts can be assembled to form highly complex structures. Yet in the macro world, gravity is the dominant force. In the microscale, however, different forces like electrostatics, intermolecular Van der Waals forces or capillary forces become predominant, which act as disturbances on the assembly process. Vision-guided control was shown to be a possibility to overcome this issue [46]. By visually sensing the probe bending, the grasp force can be controlled [47]. This led to the ability of more accurate and repeatable microassembly tasks [48]. Figure 2.2.2 shows an example of the manipulation of a microscopic part via two needle probes. With the visual guidance, the part could be inserted into the micromachined slot (lower image). This demonstrates the feasibility of vision systems aiding the development of microassembly tasks.

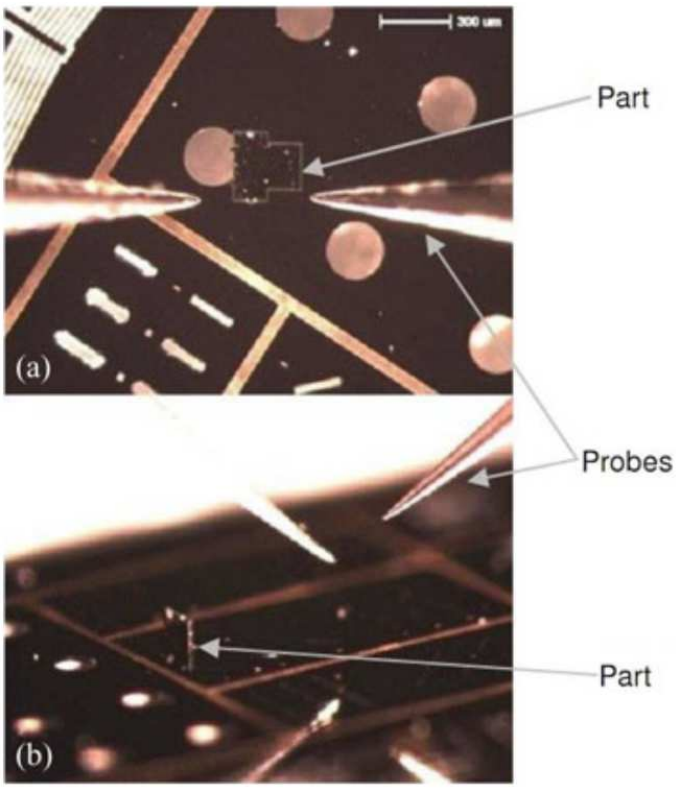


Figure 2.8: Example of a microassembly task before (top) and after (bottom) the manipulation [47].

Mechanical micromanipulation is another growing field of micromechanics. Similar to the bio-micromanipulation approach, specific probes or pipettes are used to accurately move objects in the microrange. The optimization of pick and place methods has drawn much attention, as it is widely used. Acceleration of it is the current challenge [49]. High requirements on machine vision techniques have to be met, to perform fast, yet reliable tasks. Figure 2.9(a) shows an example of a pick and place task [50]. Via enhancing the efficiency of machine vision techniques, fast and accurate execution is achieved. The borosilicat sphere is grasped, moved 60 $\mu m$ and released in under 1 s, which states the highest speed reported in literature thus far. This task is a fundamental problem for many applications. A further example is shown in Figure 2.9(b) [51]. A visually guided probe is used to place a microsphere onto an atomic force microscopy (AFM) cantilever. This results in changing its effective mass and therefore controlling its stiffness/resonance frequency.

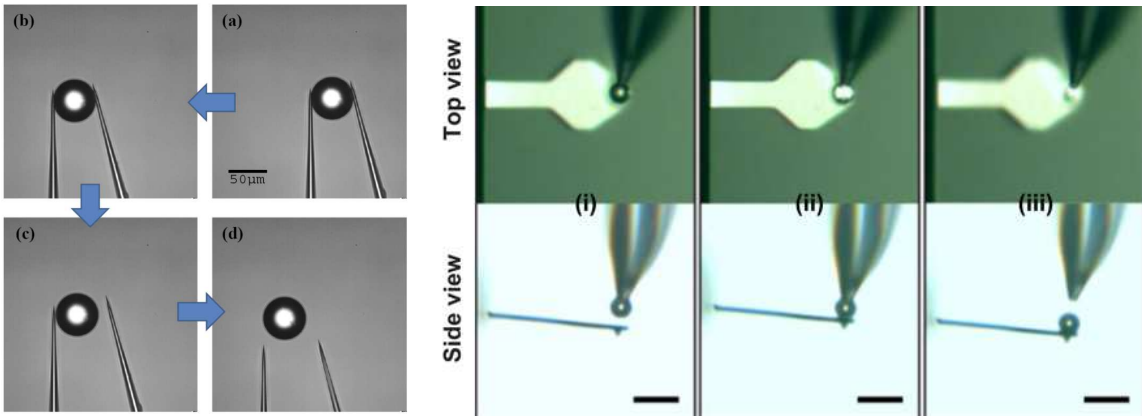


(a) (b)

Figure 2.9: (a) High-speed manipulation of a microsphere [50] / (b) Placement of a microsphere onto an AFM cantilever to tune its stiffness [51].

All in all, vision-guided systems can aid the development of various applications. It is shown that current limiting factors regarding positioning accuracy and repeatability can be overcome by the integration of specific machine vision techniques. As the promising results of other scientific fields show, this method may be an effective way to further enhance electrical probing stations.

# CHAPTER 3

# Proposed System

With the background, motivation and state of the art in mind, the proposed system is introduced in this chapter. A system overview with the main components and their specific tasks is presented. The challenges of the vertical and horizontal alignment procedures are described. An approach for the evaluation of the probe/sample positioning accuracy utilizing AFM is discussed in the last section.

## 3.1 System Overview

Figure 3.1 shows a sketch of the proposed system which is divided into three parts. The optical system describes the sensing part of the setup. Its aim is to accurately measure the position of the sample and the probe. The illumination of the light source is collimated and inserted into the optical path via a beam-splitter. An objective lens, which vertical position can be adjusted by a stepper motor, focuses the light onto the object. The reflected light hits the beam-splitter from the bottom side and the upcoming lens projects the image onto the camera sensor. By controlling the stepper motor, the spindle turns. This results in an adjustment of the objective lenses vertical position and therefore a shift of the focal plane. The counted steps provide information about the vertical position. Thus resulting in the possibility of measuring the vertical offset of the probe to the sample.
The second part of the setup is the alignment system, which moves the sample and the probe. It consists of three positioning stages. Two stages are used to adjust the horizontal position of the sample, while the third changes the vertical position of the probe. Therefore, probe and sample can be aligned with respect to each other in all three spatial dimensions.
The third part is the evaluation system, which is used to measure the positioning accuracy of the first two parts. The detailed procedure on how this is achieved is described in the last part of this chapter.

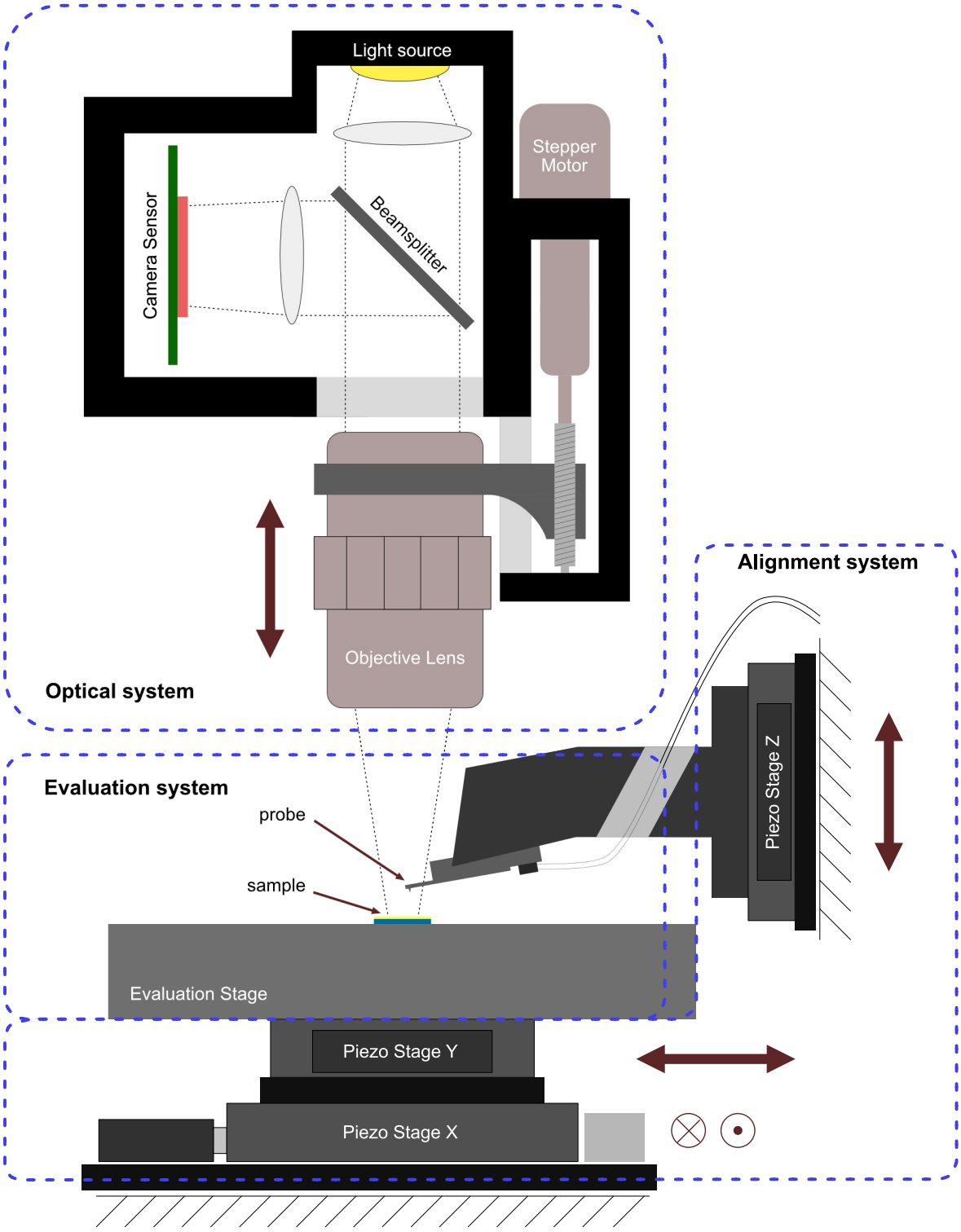


Figure 3.1: Sketch of the proposed setup, consisting of the optical system (camera, light source, beam-splitter, objective lens), the alignment system (XYZ stage) and the evaluation system (evaluation stage).

## 3.2 Vertical Alignment

By changing the position of the objective lens, the focus of the optical system can be adjusted. First, the focal plane is shifted to the probe, like in Figure 3.2(a). This can be achieved by using specific focusing algorithms, which are presented in Section 4.1. After that, focusing on the sample is done, as shown in Figure 3.2(b). The stepper motor provides information about the vertical position at each step. With that, the vertical offset of the probe to the sample can be calculated.

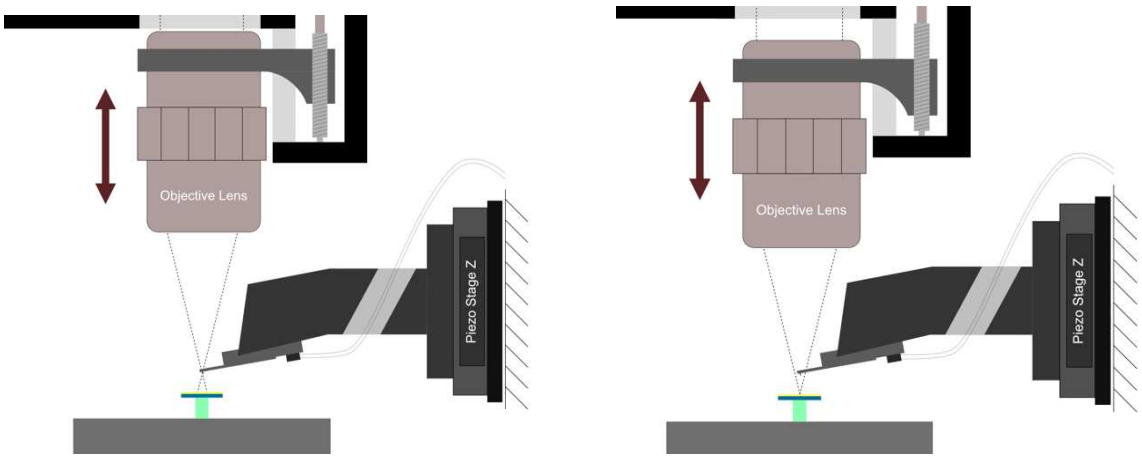


(a) (b)

Figure 3.2: Vertical position measurements.

This procedure assumes, that the moving axes of the objective lens and the Z-stage are parallel. In reality, this is usually not the case, as there is an unintended tilt. Therefore, an additional measurement is carried out. By moving the probe a bit towards the sample, this tilt can be evaluated and the vertical offset can be corrected. After the determination of the accurate vertical offset one can move the probe to the same height as the sample, by controlling the Z-stage - Figure 3.3.

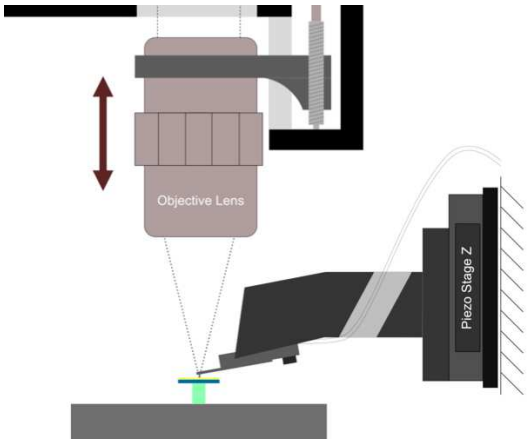


Figure 3.3: Vertical offset correction.

## 3.3 Horizontal Alignment

After compensating for vertical offset, the probe and the sample are in the same plane. The next step is the correction of the horizontal offset, which is minimized by controlling the X- and Y-stage. The initial state of the horizontal alignment is depicted in Figure 3.4(a). The position of the contact pad and the probes tip are determined using machine vision techniques, as described in Section 4.3 . The difference of these positions is proportional to the horizontal offset. By transforming this offset into positioning commands for the X- and Y-stage, it is compensated. The result is the final alignment, where the probe is contacting the contact pad - Figure 3.4(b).

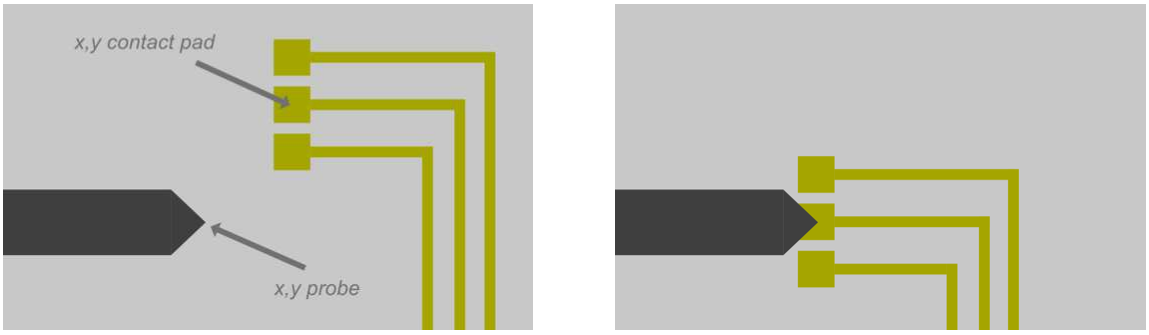


(a) (b)

Figure 3.4: Lateral alignment process / (a) depicts the position measurement of the probe and the sample / (b) shows the final alignment.

## 3.4 Evaluation of Positioning Accuracy

The physical limitations of the vertical and horizontal position detection, leads inevitably to a positioning error. This error can not be determined by the camera or implemented positioning sensors, as they are used for the alignment itself. The system has already gone to its resolution limit with the alignment procedure. An additional evaluation setup is therefore needed to be able to measure this positioning error in all three spatial dimensions. However, several points need to be considered when implementing such an evaluation setup. First, the resolution of the sensing part needs to be at least an order of magnitude lower than that of the alignment system. With a possible positioning offset in vertical as well as in horizontal direction, the setup should be able to measure the offset in all three spatial dimensions. As a last point, the measurement should not disrupt the alignment in order not to falsify the results.

Figure 3.5(a) shows the finished alignment utilizing a standard needle-probe. It is clear that the determination of $\Delta x$, $\Delta y$ and $\Delta z$ is rather hard in this case. Therefore, a replacement of the needle-probe by a cantilever-probe with integrated deflection sensors is proposed in this work - Figure 3.5(b).

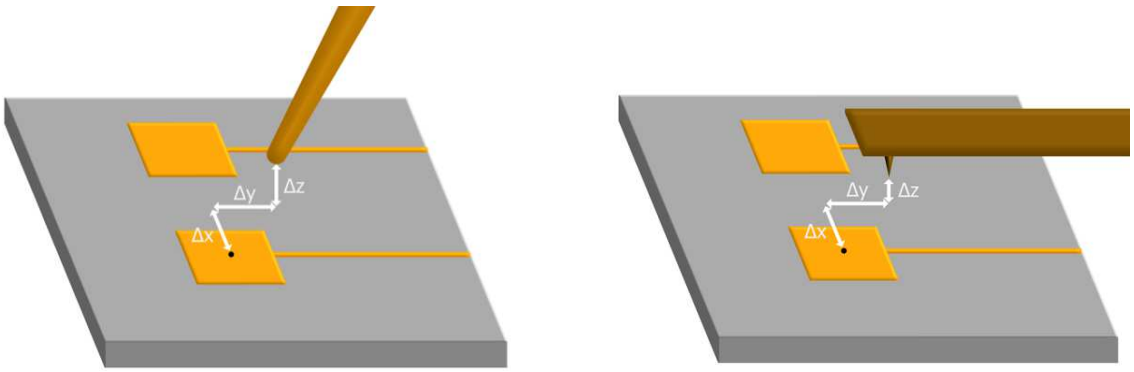


(a) (b)

Figure 3.5: Replacement of an actual probe with an AFM cantilever.

Such probes are already used in other scientific fields and applications, such as AFM [52]. The integrated deflection sensors enable the measurement of the vertical positioning error $\Delta z$ with nanometer resolution. For the determination of the horizontal positioning error, this idea can be expanded. By moving the sample in the horizontal directions, the cantilever-probe deflects corresponding to the samples topography. This results in the ability of scanning the samples surface. For this purpose an additional XY-evaluation stage is integrated into the system (see Figure 3.1). The resulting topography image of the sample then provides information on the horizontal positioning offset $\Delta x$ and $\Delta y$.

# CHAPTER 4

# Theoretical Background

This chapter discusses the theory of automatically vision-guided alignment systems. After showing how focusing in computer microscopy is achieved in literature, lateral object detection methods are described. The theory and working principle of AFM is introduced in the last section.

## 4.1 Focusing

Focusing can be divided in active and passive focusing methods. Active focusing uses additional hardware to measure the distance to the object. This information is then used to adjust the position of the objective lens and therefore the focal plane. The distance measurement is usually done via time of flight sensors and finds application in various commercially available cameras. Passive methods are used to determine the distance from the image that is acquired at the camera sensor. It includes methods such as phase detection and contrast detection. Phase detection is the most commonly used technique in photography as it is rather fast [53]. However, additional hardware is used, as the incoming light is divided into two images. From these images the phase difference and therefore the quality of the focus is determined.
Contrast based focus detection uses the intensity difference of adjacent pixels, which increases naturally with correct focus. With better focus, the diameter of the circle of confusion (CoC) gets smaller thus less blurring of the image happens. This can be modelled as a convolution of the image with a gaussian kernel [54, 55]:

$$h(x,y) = \frac{1}{2\pi\sigma^2} exp\left(-\frac{x^2+y^2}{2\sigma^2}\right) , \tag{4.1}$$

where the standard deviation $\sigma$ is proportional to the CoCs diameter. Figure 4.1 visualizes the dependence of the CoC on the focus offset. The blue rays depict a correctly focused object at a distance $S_1$ from the lens. It is projected onto the image

plane with a diameter of the CoC c = 0. However, if the object shifts to the position $S_2$ (red rays), c gets bigger, resulting in a blurred image. As this method does not require additional hardware, it is often used in the field of computational microscopy.

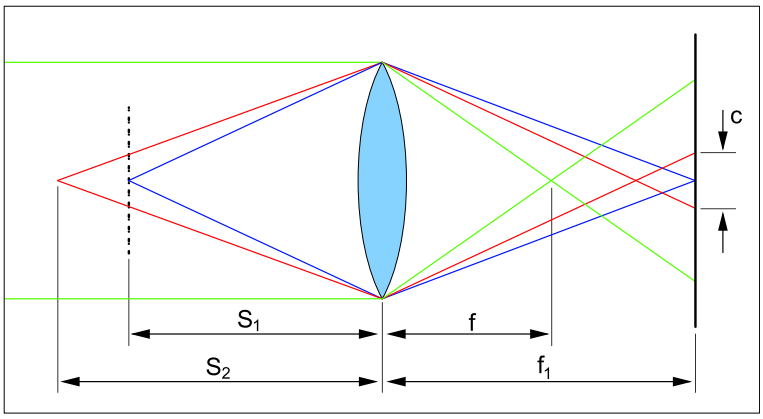


Figure 4.1: Circle of confusion.

Yet, there exist many methods to calculate the focus score of an image. An overview can be found in [56] and [57]. All of them mainly rely on the high frequency content of the processed images. Differences in weighting functions or image filters make each of them applicable to different types of microscopy, like noisy environments or lower resolution images. Some of them are presented here:

1. Tenenbaum Gradient (Tenengrad):

   This method convolves the image $i(x, y)$ with sobel operators $S_x$ and $S_y$ in x and y direction, respectively:

$$S_x = \begin{bmatrix} 1 & 0 & -1 \\ 2 & 0 & -2 \\ 1 & 0 & -1 \end{bmatrix}, \qquad S_y = \begin{bmatrix} 1 & 2 & 1 \\ 0 & 0 & 0 \\ -1 & -2 & -1 \end{bmatrix}. \tag{4.2}$$

   The resulting image gradient magnitudes $G_x$ and $G_y$:

$$G_x(x, y) = i(x, y) * S_x \ , \qquad G_y(x, y) = i(x, y) * S_y, \tag{4.3}$$

   are then squared and summed up by the following Equation. H and W are the height and width of the image, respectively:

$$F_{Tenengrad} = \sum_H \sum_W G_x(x, y)^2 + G_y(x, y)^2 \ . \tag{4.4}$$

   Figure 4.2(a) and 4.2(b) show an example image before and after convolution with the sobel operators. This method basically calculates the edge image. In conclusion, the image with the strongest edges is the image in focus.

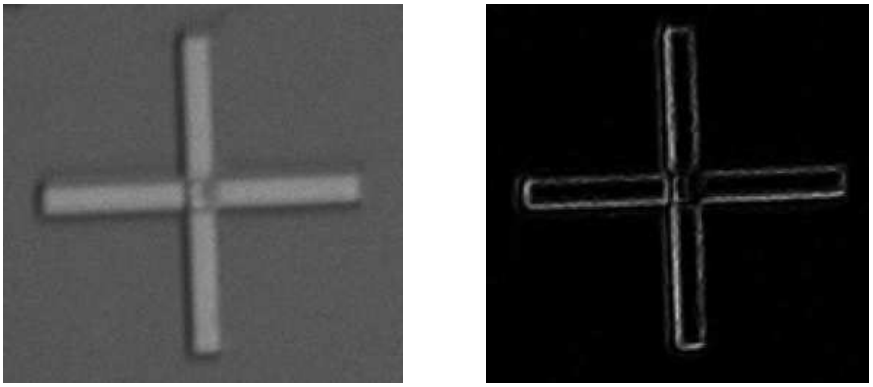

(a) (b)

Figure 4.2: (a) acquired image, (b) computed edge image via convolution with sobel operators.

2. Tenenbaum Variance (Tenenvar):

   Similar to the method above, this technique computes the variance of the edge image:

$$F_{Tenenvar} = \sum_{H}\sum_{W}[S(x,y) - \bar{S}]^2 \ , \qquad S(x,y) = \sqrt{G_x(x,y)^2 + G_y(x,y)^2} \ , \quad (4.5)$$

   where $\bar{S}$ denotes the mean intensity of $S(x,y)$.

3. Normalized variance:

   This method computes the normalized variations in grey level among all image pixels:

$$F_{normed\ variance} = \frac{1}{H * W * \mu}\sum_{H}\sum_{W}[i(x,y) - \mu]^2 \ , \quad (4.6)$$

   where $\mu$ is the mean intensity of the image $i(x,y)$. This method compensates for the differences in average image intensity among different images.

4. Squared gradient:

   This method sums the squared gradient, making larger gradients more important:

$$F_{squared\ gradient} = \sum_{H}\sum_{W}[i(x+1,y) - i(x,y)]^2 + [i(x,y+1) - i(x,y)]^2 \quad (4.7)$$

5. Brenner gradient:

   Similar to the squared gradient, this technique computes the gradient with a vertical/horizontal distance of 2:

$$F_{brenner\ gradient} = \sum_{H}\sum_{W} [i(x+2,y) - i(x,y)]^2 + [i(x,y+2) - i(x,y)]^2 \quad (4.8)$$

By scanning along the optical axis and constantly calculating the focus score, one receives a focus curve with a maximum at its best focused position. The comparison of the focus curves of the introduced methods is shown in Section 6.1.2 and is based on the following parameters:

- Accuracy: Distance between the object plane to the maximum of the focus curve.
- Number of false maxima: This parameter describes the number of false maxima in the focus curve, besides the global maximum.
- Width: The full width at half maximum (FWHM) describes the sharpness of a function. Big FWHM means good global detection, while a small FWHM results in good local peak detection.
- Noise: Robustness against possible pixel noise and other parasitic effects.
- Execution speed: Duration of calculating the focus score of an image.

As shown in Chapter 2, faster execution of the vision-guided automation is a key step to further increase the applicability. In order to minimize the duration of finding the maximum of the focus curve, several peak-searching algorithms are presented.

## 4.2 Fast Peak Searching Algorithms

By scanning along the optical axis and constantly capturing images and calculating the focus score, one receives a focus curve. The maximum of this curve depicts the best focused image. In order to rapidly find the maximum of this curve, several fast peak-searching algorithms were developed [58]. The five most common methods are presented here:

1. Fixed stepsize search

   As the name states, the focus score is calculated at fixed step sizes. With a range $l$ and a targeted accuracy $\alpha$, the number of required image captures $N$ can be calculated as:

$$N = \left\lceil \frac{l}{\alpha} + 1 \right\rceil . \quad (4.9)$$

   The method exhibits relatively long computation times, as the aimed accuracy is usually at least an order of magnitude lower than the scanning range. This results in a rather large number of required images $N$.

2. Fixed stepsize search with interpolation

   Interpolation of the captured values can help to increase the speed, while maintaining the accuracy. However, linear or quadratic interpolations do not perform well on focus curves, resulting in the need for more complex interpolation models. The advantage of a reduced number of required images is bought by the more computationally expensive fitting algorithm.

3. Iterative search

   This method makes several sweeps to find the focus peak. From sweep to sweep the step size and search range are gradually decreased. The number of required image captures can be calculated as:

$$N = \left\lceil \eta \frac{log(\alpha/l)}{log(2/(\eta-1))} \right\rceil , \tag{4.10}$$

   where $\eta$ is the number of captures per sweep. Figure 4.3 visualizes the iterative search with $\eta = 6$. The first sweep acquires $\eta$ images at equidistant steps over the whole range. By calculating the focus scores and evaluating their maximum, the range of the second sweep is adjusted to the upper and lower step of the previous maximum.

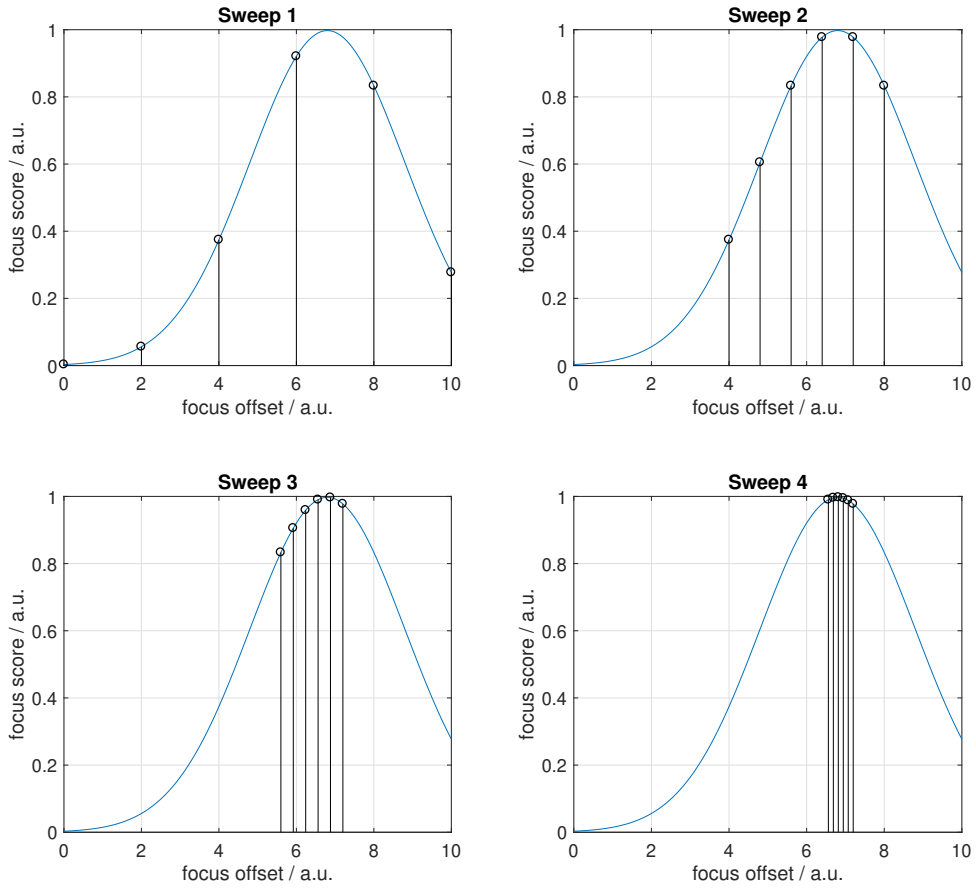


Figure 4.3: Visualization of the iterative search algorithm.

This procedure is repeated, till the stepwidth is smaller than the aimed accuracy $\alpha$.

4. Variable stepsize search / Rule based search

   Several rule based peak searching algorithms were developed [59, 60]. Rule based refers to the development of a focus score dependent stepsize, based on a reference focus curve. This method provides high focusing accuracy at a rather low execution time. The actual amount of required images varies from the initial stepsize and specific focus curve. As the stepsize is depending on the focus curve, different focusing times throughout different objects are the result.

5. Fibonacci search

   This method is a special case of the iterative search as the range changes from sweep to sweep. Four initial captures at 0%, 38.2%, 61.8% and 100% of the range (golden cut) are taken on the first iteration. Similar to the iterative search, the range of the upcoming sweep is adjusted around the maximum. As the values at 0%, 100% and either 38.2% or 61.8% are now already known, only one additional scan is required at each further iteration. This leads to a fast and accurate convergence in focus position. Figure 4.4 illustrates this procedure.

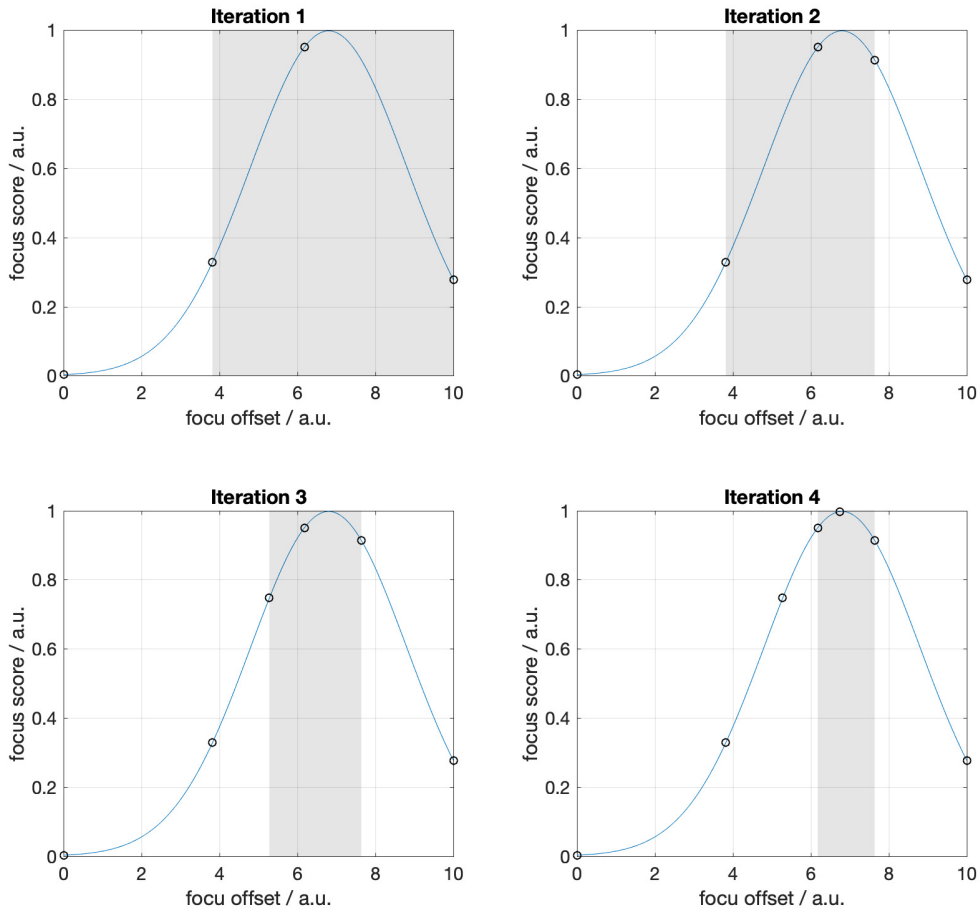


Figure 4.4: Visualization of the fibonacci search algorithm.

The gray region is the adjusted scanning range for the upcoming iteration. As three points are already known from the previous scan, only one needs to be carried out to move on to the next step.

## 4.3 Horizontal Detection

The extraction of features of interest from the acquired images is a key step in vision-guided systems. The state of these features, such as position or orientation of an object, is then used to control actuators. This control through continuous vision-feedback is known as visual servoing. The steady observation of an object is commonly referred to as visual tracking. This tracking involves the usage of machine vision techniques to detect features of a known object, like corners or edges, to thereby obtain further knowledge about its position [61]. Yet, there exist many techniques to find an objects XY-position in an image, each of them is specialized to different tasks. An overview can be found in [62, 63]. For example, optical flow or frame differencing methods [64] are capable of finding moving objects, while silhouette or kernel based techniques [65], can locate an object based on its shape.
This work focuses on the position detection of a probes tip and contact pads of ICs, which have straight lines, pronounced edges and almost no texture. Additionally, repeating structures, like pad-corners can occur. Dust particles, which can accumulate on the ICs surface and trigger false results, also need to be taken into account, thus making standard feature detectors like SIFT [66] or SURF [67] unusable. Silhouette or kernel based feature matching algorithms provide a robust detection of objects which is insensitive to arbitrarily shaped dust particles. They are therefore well suited for this task.
Silhouette based algorithms use color histograms, contour or edge distributions of an object, to find its position in an image. After extracting the contour information of an image it gets matched to the contours of the template object, which leads to the location of the object. Via gradient descending techniques tracking of an object can be achieved [68]. However, kernel-based techniques are used more often due to their ease of implementation, high detection accuracy and robustness against noise [69]. The most common technique amongst them is called template matching. It is also featured in other vision-guided systems as discussed in Section 2.2.

### 4.3.1 Template Matching

Finding the Pixel-Coordinates of an object using template matching is achieved by computation of the normalized cross correlation of the image f(x,y) and a template t. Equation (4.11) shows the used formula for computing the normalized cross correlation $\gamma$ at a pixel (u,v):

$$\gamma(u,v) = \frac{\sum_{x,y}[f(x,y) - \overline{f}_{u,v}][t(x-u,y-v) - \overline{t}]}{\sqrt{\sum_{x,y}[f(x,y) - \overline{f}_{u,v}]^2 \sum_{x,y}[t(x-u,y-v) - \overline{t}]^2}} \,. \tag{4.11}$$

Figure 4.5(a) visualizes this process. By shifting the template (top left patch) over

the image and calculating the correlation at each pixel one receives a matching image - Figure 4.5(b). The maximum in the received function results in the coordinates of the matched object (black mark).

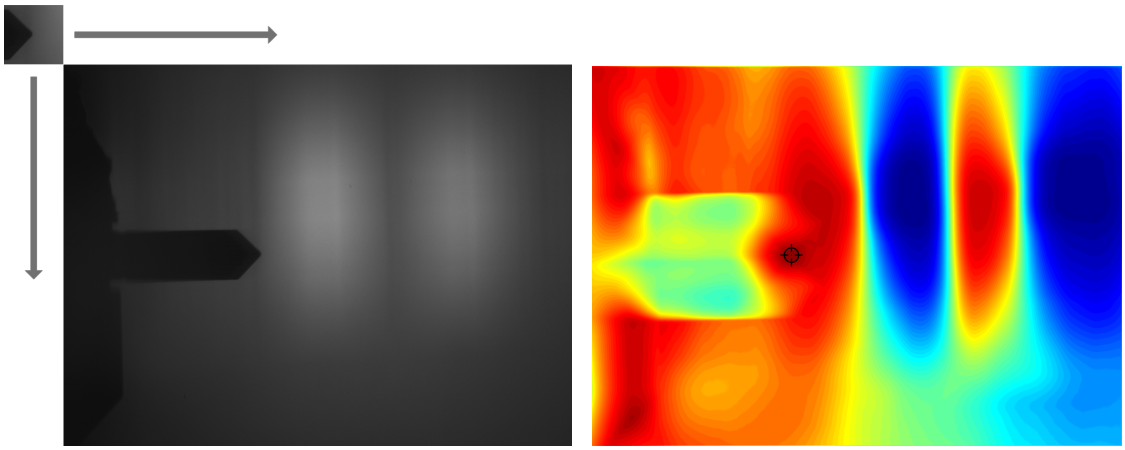

(a) (b)

Figure 4.5: Visualization of the template matching technique. / (a) captured image with template / (b) template matching result.

Template matching has the advantages of robustness against noise and high accuracy, thus making this method reliable. However, as the task needs long computation times, the ability of real-time tracking of an object is limited. The influence of the execution speed on the overall alignment procedure is analyzed in Section 6.2.

## 4.4 Atomic Force Microscopy

Atomic force microscopy is a type of a scanning probe microscope, which can resolve the topography of an investigated sample down to the nanometer range. Special forms of AFMs exist for different purposes like biological, mechanical or electromagnetical sample characterization. The common task of the various variants is the scanning of a probe, further referred to as cantilever, over the investigated sample. The cantilever is deflected by interaction forces, such as intermolecular Van der Waals-, electrostatic- or capillary-forces. This results in the ability of sensing the samples topography (standard AFM), electric charge distribution (kelvin probe force microscopy (KPFM)) [70] or magnetic properties (magnetic force microscopy (MFM)) [71].
The important application for this work is the topography measurement. This can be achieved via several approaches, like contact- or tapping-mode. For their ease of implementation piezoresistive cantilevers in contact mode were chosen [72]. Other than the conventional optical approach, no additional hardware than the scanning stage and the cantilever itself is used. Figure 4.6 shows a general working scheme of an AFM. The investigated sample sits on a 3-dimensional positioning stage. A, piezoelectric stage with integrated capacitive sensors is used, which enables accurate and fast positioning in the nanometer range. A high- and a low-frequency triangular scan trajectory is

applied to the X- and Y-stage, respectively. The combination of this trajectories and the samples topography lead to the deflection of the cantilever in Z-direction. This deflection changes the resistance of the piezoresistive elements on the cantilever, which are detected using a bridge circuit and converted into an output signal.

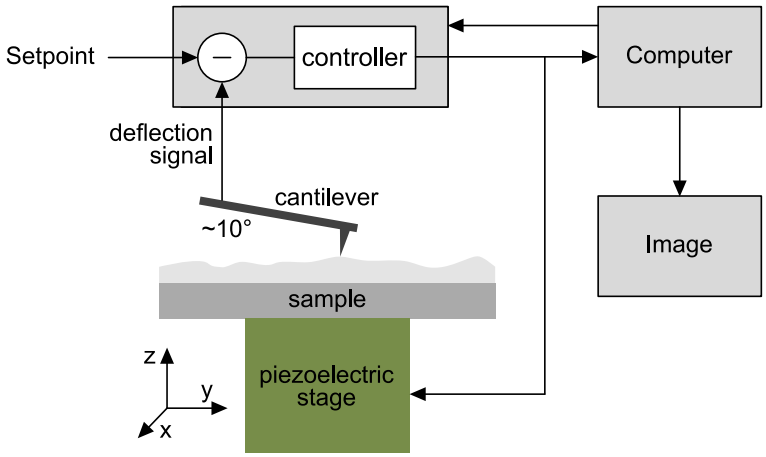


Figure 4.6: General AFM scheme.

This output signal is then compared to a specified setpoint. If a deviation occurs, the controller sets an adjusted output for the Z-stage in order to minimize it. This process is repeated till the whole range in X- and Y-direction is scanned. The result is four signals, namely the scanning trajectory in X- and Y- direction, the output signal for the Z-stage and the cantilever deflection signal. From these signals the topography and error images of the sample can be calculated. Figure 4.7 depicts an example AFM image of a silicon calibration grating. The topography image (A) and error image (B) correspond to the signal of the Z-stage and the cantilever deflection, respectively.

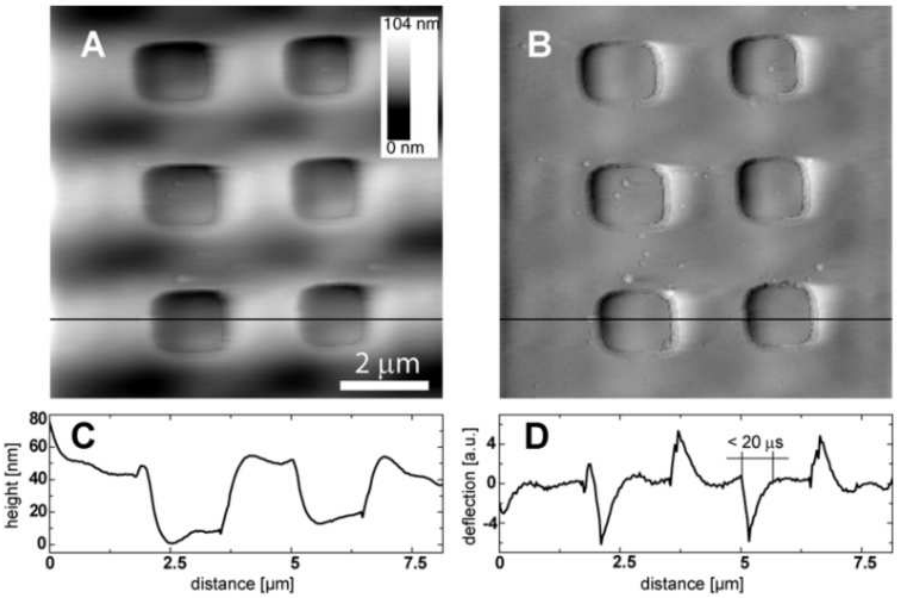


Figure 4.7: example AFM topography / error image of a silicon calibration grating [73].

# CHAPTER 5

# Implementation

This chapter presents the implementation of the actual system. First a general overview using a block diagram is given. The interaction between all components will be discussed. Based on their parameters, the chosen components are introduced. A look on the utilized test sample and images of the real implementation finish this chapter.

## 5.1 System Overview

Based on the general system sketch of Section 3.1, Figure 5.1 shows the block diagram of its implementation, which is divided into two parts. The main part, the aim of which is the alignment of the probe to the sample (left part) and the evaluation part, the aim of which is the measurement of the positioning accuracy (right part). Both of those parts share the "System" Block, which is the core of the whole setup, and are manipulating it. It consists of all the main components, such as optical system, alignment stages and evaluation stages, all of which are presented in the upcoming sections.
The alignment procedure is implemented on a conventional PC (Main PC). Its task is to communicate with all the peripherals and execute the programmed algorithms. The change in focus is achieved by communicating with the stepper motor controller via UART. The acquired images from the camera are sent to the PC via a USB connection. The control of the three alignment stages is done via separate serial UART interfaces. The underlying control loop is executed on its own stage controller, which ensures that the positioning commands are met at all times. A data acquisition (DAQ) card, which acquires the deflection signal from the AFM cantilever is connected to the main PC as well. Its main task is to ensure that the tip will not be damaged during the alignment process.

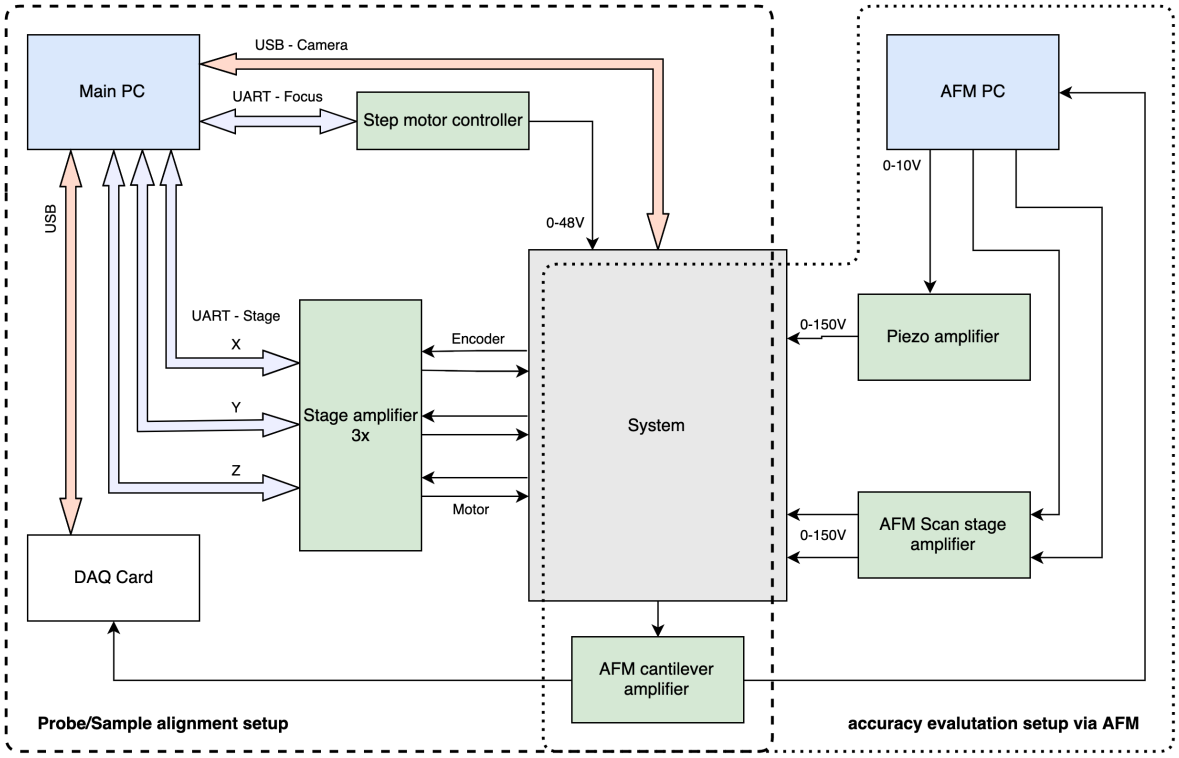


Figure 5.1: Blockdiagram depicting the most important components.

The second setup is the AFM for the determination of the positioning accuracy. It consist of a real time capable PC (AFM PC) which executes an implemented Matlab/SIMULINK model. Two triangular scanning paths are generated and sent to the AFM scanning stage amplifier (fast scan axis / slow scan axis). By measuring the deflection signal of the cantilever a Z-piezo is controlled via an amplifier. By keeping the deflection constant, a topography (Z-piezo signal) and an error (tip deflection signal) image can be created. Theses images then lead to the positioning accuracy. A more detailed explanation on how this is achieved can be found in Appendix A.

## 5.2 Used Components

This section introduces the most important components used in this thesis. All parameters are presented and their impact on the overall system performance is discussed. After a look on the optical, the alignment and the evaluation system parts, the used test sample is presented. Images of the whole compound setup will be described in the last section.

### 5.2.1 Objective Lens

The objective lens magnifies the image onto the camera sensor. A large magnification and low depth of field (DOF) is aimed to increase the accuracy of the system. 20x or 50x objective lenses usually have a distance to the samples surface (= working distance) of few millimeters. This working distance is inverse proportional to the magnification and numerical aperture (NA). However, the proposed setup needs some room for the probe to move to avoid damage of itself and the objective lens. Additionally, a sufficient vertical range for focusing is required. As a tradeoff between working distance and NA, a long working distance objective lens (10x Mitutoyo Plan Apo Infinity Corrected Long WD Objective, Edmund optics, Germany) is chosen. The parameters can be found in Table 5.1:

Table 5.1: Objective lens parameters.

| | |
|---|---|
| Magnification | 10x |
| NA | 0.28 |
| Working distance | 34 mm |
| Type | Infinity corrected |

With a NA of 0.28 and a refractive index of $n = 1$ (air), Equation (5.1) leads to the corresponding opening angle:

$$\theta = arcsin\left(\frac{NA}{n}\right) = arcsin\left(\frac{0.28}{1}\right) = 16.26° \ . \tag{5.1}$$

The type 'Infinity corrected' means, that the exiting light beam of the lens is collimated. This leads to the ability of easily integrating a custom light source into the optical path via a beamsplitter. A white LED (GW PSLM31.EM-GUHQ-A131-1, Osram, Germany) is chosen. However, as the beam is collimated, an additional tube lens with a magnification of 0.5x is necessary to project the image onto the camera sensor, resulting in an overall magnification of 5x. With the chosen objective lens and light source, the DOF is calculated as follows:

$$DOF = \frac{\lambda}{2 * NA^2} = \frac{550nm}{2 * 0.28^2} = 3.5\mu m \ . \tag{5.2}$$

As the light source is white, Equation (5.2) uses a wavelength of 550 nm (green light), which corresponds to the middle of the visible light spectrum. With a DOF of 3.5 $\mu m$, this objective lens allows the aimed vertical position detection in the micrometer range, while maintaining a practicable working distance.

### 5.2.2 Camera

The camera is used to record the magnified image. A monochrome camera (DMM 72BUC02-ML, The Imaging Source, Germany) with a CMOS sensor is used. The parameters are listed in Table 5.2:

Table 5.2: Camera parameters.

| | |
|---|---|
| Maximum resolution | 2592 x 1944 (5 Megapixel) |
| Frame rate | 6 FPS @ max. resolution |
| Format | 1\2.5 inch |
| Pixel size | 2.2 $\mu m$ x 2.2 $\mu m$ |
| Sensor size | 5.7 mm x 4.28 mm (7.13 mm diagonal) |

The usage of the maximum resolution is desired for high accuracy. However, the frame rate of 6 frames per second (FPS) means long computation time. As a tradeoff, the CMOS sensor enables the possibility to increase the frame rate by implementing several techniques. The time-limiting factor of the camera is the readout circuit of each pixel. By decreasing the amount of pixels to be read out (by specifying a region of interest (ROI)) the number of FPS increases, while maintaining the high resolution. Additionally, for non-resolution-critical steps, several pixels can be combined to one. This results in a higher frame rate, yet lower resolution. By using Equation (5.3), the field of view (FOV) of the system can be calculated:

$$FOV = sensor\ size * \frac{1}{magnification} = \begin{bmatrix} 5.70mm \\ 4.28mm \end{bmatrix} * \frac{1}{0.5} * \frac{1}{10} = \begin{bmatrix} 1140\mu m \\ 856\mu m \end{bmatrix} . \quad (5.3)$$

The achieved FOV is reasonably large enough to maintain an overview of the sample. The real world pixel size (RWPS) describes the size of a square in real world coordinates which is represented by one pixel. It can be calculated as follows:

$$RWPS = \frac{sensor\ size}{camera\ resolution * magnification} = \frac{5.7mm}{2592 * 5} = \frac{4.28mm}{1944 * 5} = 0.44\mu m . \quad (5.4)$$

Therefore, using the maximum resolution, 1 pixel in image coordinates represents a 0.44 $\mu m$ square in real world coordinates. This parameter can be enhanced using higher resolution and smaller sensor size resulting in a smaller pixel size. However, pixel sizes are limited by manufacturing techniques and a higher resolution will result in even lower frame rates. This camera offers a tradeoff between these parameters, while allowing a real world resolution in the micrometer range.

### 5.2.3 Alignment Stages

The used alignment stage consists of a piezoelectric linear motor (HR4-K-S-3, Nanomotion, Israel) which is controlled by a custom built controller and an amplifier (AB5 driver amplifier, Nanomotion, Israel). With the targeted and the current position, sensed by an incremental encoder (RGH24H30D30A, Renishaw, Land), the amplifier adjusts the output signal for the motor. The parameters of the combined alignment stage are shown in Table 5.3:

Table 5.3: Alignment stage parameters.

| | |
|---|---|
| Resolution | 50 nm |
| Range | 4.6 cm |
| Controller frequency | 20 kHz |
| Max. speed | 250 $^{mm}/_{s}$ |
| Communication protocol | UART |

In the whole setup, three stages will be implemented. Two for XY-positioning of the sample and one for Z-positioning of the probe. The parameters of the stage are chosen to not be the limiting factor of the alignment (Resolution: 50 nm $<$ camera RWPS: 0.44 $\mu m$). A range of 4.6 cm is enough for the alignment of the 1x1 $cm^2$ sample and suitable for the movement of the probe along the working distance of the objective lens ($=$ 34 mm). Additionally, in comparison to the frame rate of the camera (6 FPS), the controller frequency of 20 kHz and a maximum stage speed of 250 $^{mm}/_{s}$ ensure fast positioning.

### 5.2.4 Stepper Motor for Focus Control

The objective lens is mounted on a spindle (M1.6 x 0.35 x L1, Faulhaber, Germany). By rotating it with a stepper motor (AM1524, Faulhaber, Germany), its vertical position is controlled. The stepper motor itself is actuated by a control circuit board (EVAL6470h-DISC, STMicroelectronics, Netherlands), which receives positioning commands via a UART connection from the main PC. A micro-step mode of 1/128 increases the initial 24 $^{steps}/_{rotation}$ of the stepper motor up to 3072 $^{steps}/_{rotation}$. With a spindle pitch of 350 $^{\mu m}/_{rotation}$, the achieved vertical positioning resolution of the objective lens is 113.9 $^{nm}/_{step}$.

$$Resolution = \frac{spindle\ resolution}{stepper\ motor\ resolution} = \frac{350\frac{\mu m}{rotation}}{24\frac{steps}{rotation} * 128} = 113.9\frac{nm}{step} \tag{5.5}$$

Table 5.4: Parameters of focus control setup.

| | |
|---|---|
| Resolution | 113.9 $^{nm}/_{step}$ |
| Range | 5 mm |
| Max. speed | 1 $^{mm}/_{s}$ |
| Communication protocol | UART |

The step size of 113.9 $^{nm}/_{step}$ is significantly smaller than the DOF of the objective lens ($=$ 3.5 $\mu m$), thus not limiting the focusing accuracy. Additionally, a range of 5 mm is suitable for focusing on the sample and the probe. Yet this configuration has a limited speed of 1 $^{mm}/_{s}$, it provides a tradeoff regarding the high resolution.

### 5.2.5 AFM Cantilever / Stage

The utilized AFM is composed out of a self-sensing cantilever and a three-dimensional scanning stage. The cantilever (PRSA-L300-F50-Si-PCB, SCL Sensortech, Austria) has integrated piezoresitive elements, configured in a bridge circuit, allowing for the detection of small deflections. Its parameters are shown in Table 5.5.

Table 5.5: AFM cantilever parameters.

| | |
|---|---|
| Silicon tip radius | 15nm |
| Sensitivity | 1-2 $^{\mu V}/_{nm}$ |
| Dimensions | L = 305 $\mu$m / W = 110 $\mu$m |

A scanning electron microscope (SEM) image of the cantilever is shown in Figure 5.2. As the optical system looks on the cantilever from the top, the actual tip which is in contact with the sample can not be observed. Therefore an offset of 10 $\mu m$, determined from the SEM image, is taken into account to minimize the positioning error.

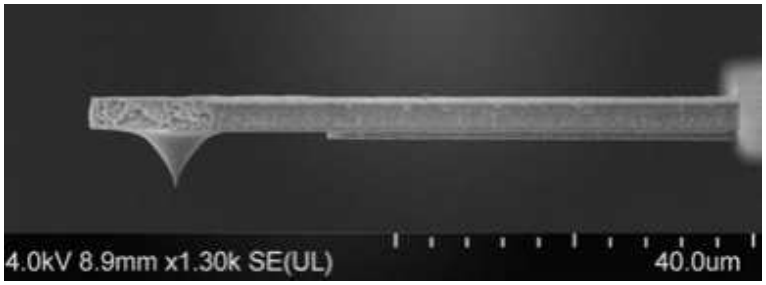


Figure 5.2: SEM image of the implemented piezoresistive cantilever [74].

Besides the cantilever, the AFM consists of a scanning stage and its controller. The stage, which moves the sample in a specific trajectory is composed of a XY-Stage (NPXY100-100, nPoint, USA) and its controller/amplifier (LC.402 (2-Channel), nPoint, USA). Via capacitive sensors integrated into the stage, the position is controlled. Table 5.6 shows its parameters.

Table 5.6: AFM stage parameters

| | |
|---|---|
| Max. scanning range | 100 $\mu m$ x 100 $\mu m$ |
| Controller frequency | 40 kHz |
| Position noise | 0.3 nm |

A piezo stack actuator (NAC2013-H08, Noliac, Denmark) is used for vertical Z-positioning of the sample. The used amplifier (Techproject, Austria) delivers output voltages of 0-150 V, which corresponds to an expansion of 0-8 $\mu m$.

### 5.2.6 Realtime PC

A real time capable PC is used to implement the AFM controller. An ADC board (DS2004, dSpace, Germany) converts the measured voltages (cantilever deflection, measured scan trajectory) to signals which can be interpreted by the processor board (DS1005, dSpace, Germany). The implemented controller scheme, which is explained in more detail in Appendix A, is evaluated at a frequency of 20 kHz. The resulting signals (adjusted Z-piezo voltage, scan trajectory) are output via a DAC board (DS2102, dSpace, Germany).

## 5.3 Test Sample

The used sample for test purposes is a standard 1x1 $cm^2$ silicon substrate. With a commonly used lithography process a sacrificial photoresist layer is structured and developed. A metal stack composed of 10 nm titanium (for adhesion purposes) and 150 nm gold is evaporated and structured via a lift-off process. The resulting structure has a height of 160 nm and has various test patterns with different dimensions, as shown in Figure 5.3.

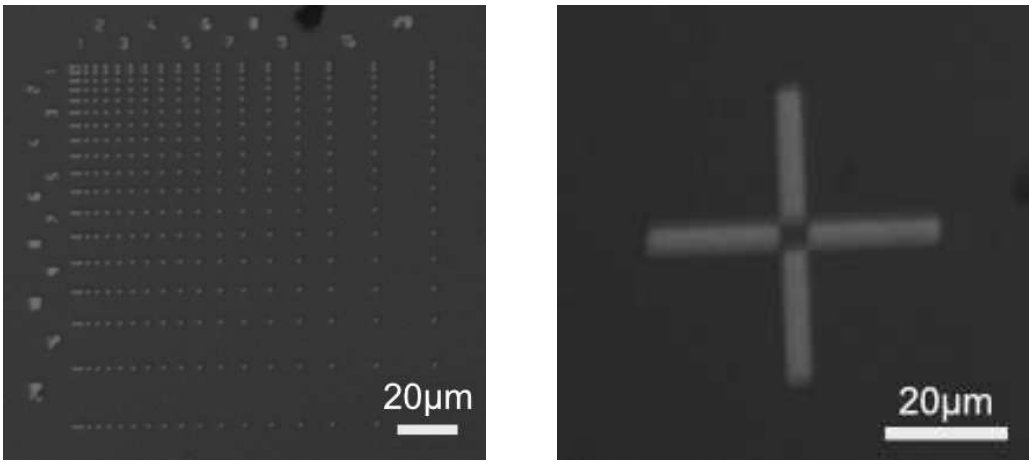


(a) (b)

Figure 5.3: (a) test structure | dots with different spacing / (b) marker for mask alignment.

Subfigure (a) shows gold dots with a diameter of 1 $\mu m$ and variable spacing of 1-20 $\mu m$ on silicon substrate. Subfigure (b) shows an alignment marker, the purpose of which is to aid the alignment of lithographic masks in the manufacturing process. Several tens of those markers are scattered on the samples surface. These structures are suitable due to their small dimensions and are used throughout the work for the probe/sample alignment process.

## 5.4 Real Implementation

All above listed components are implemented in the whole setup depicted in Figure 5.4. The left image shows the core of the whole system, from the three alignment stages, the optical system (objective lens + camera) to the evaluation part, consisting of the AFM Stage and piezoresistve cantilever.

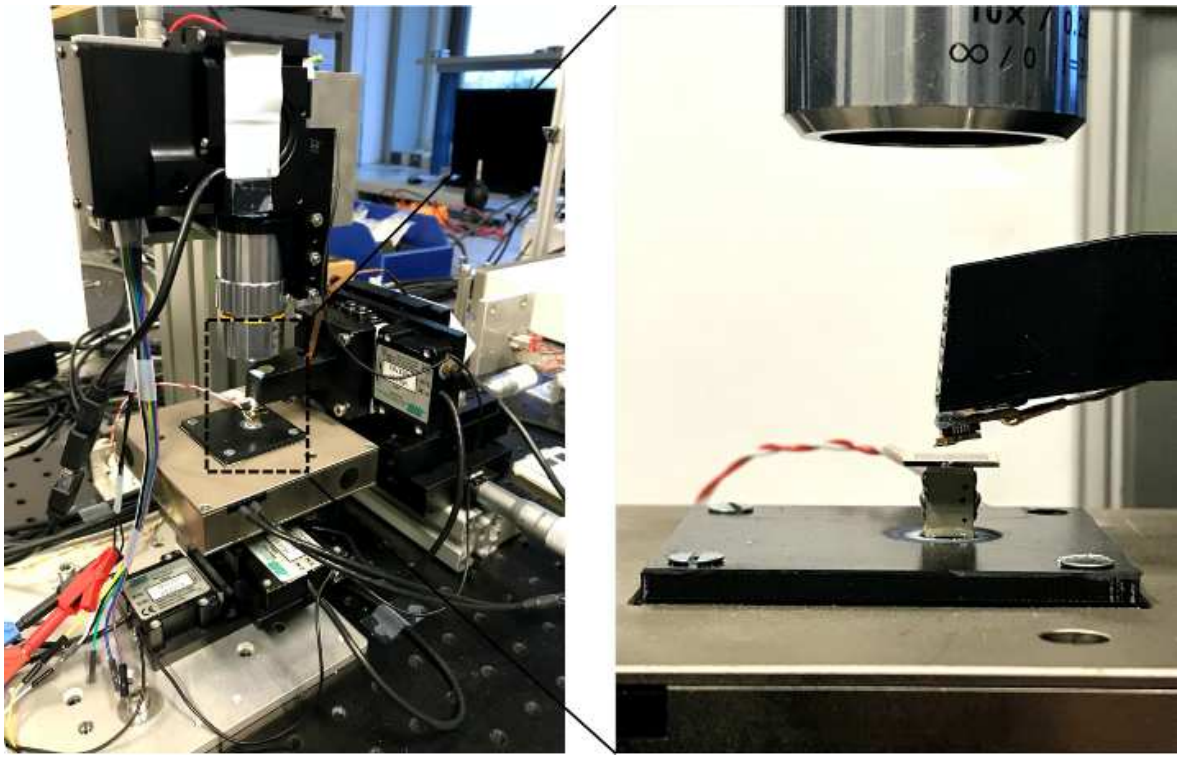

Figure 5.4: Real world implementation with a detailed view on the system-core. The objective lens, AFM cantilever, sample, Z-Piezo and the AFM stage are shown (from top to bottom).

The right image shows a more detailed view on the probe/sample alignment itself. The sample, which sits on the Z-Piezo, is observed via the objective lens (top). By controlling the XY-position of the sample and the Z-position of the cantilever (mounted on a 3D printed part) alignment is carried out.

# CHAPTER 6

# Test Procedures and Results

This chapter is divided into two parts. First, the measurement routine and results for the evaluation of the vertical positioning accuracy are presented. The horizontal alignment procedure with its evaluation system is described in the second part. The chapter finishes with alignment experiments, where different camera resolution are compared.

## 6.1 Vertical Alignment

As discussed in Chapter 3 the alignment process is divided into two parts. First, by measuring the Z-positions of the cantilever and the sample, vertical alignment is achieved. This section discusses the detailed measurement procedure and presents the positioning accuracy results in vertical direction.

### 6.1.1 Procedure

Section 4.1 already discusses the theory and used algorithms behind focusing. For a given image each algorithm returns a focus score $F_s$. The goal is now to change the vertical position of the objective lens in order to maximize $F_s$. As there are two objects in the focusing direction (probe and sample) one needs to find both maxima to calculate the vertical offset. With a step size of 113.9 nm, a frame rate at max. resolution of 6 FPS and a range of 5 mm, a fixed stepsize search would last around two hours. Therefore, a two-step focusing procedure is carried out. First, a coarse scan at lower resolution and bigger stepsize is done to find the approximate vertical position of the probe and the sample. After that, a fine scan at these specific positions is done to accurately measure the vertical offset.
Figure 6.1 shows an example of the fast scan over the whole range. A resolution of 648x484 with a framerate of 24 FPS and a stepsize of 50 $\mu m/_{\text{image}}$ is chosen. Therefore,

the scan over the whole 5 mm range lasts around 4 s. The choice of the focus algorithm has a rather small influence on the coarse scan result and will be discussed later.

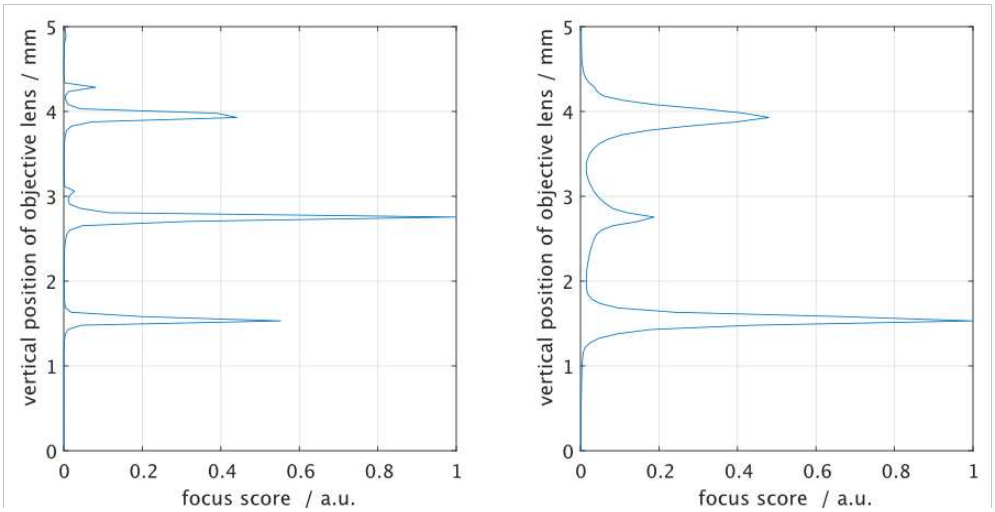


Figure 6.1: Scan over the whole range and measured focus-score using tenenbaum gradient/ without (left) and with (right) intentional gaussian blur.

Due to the reflectivity of the sample (gold layer / flat silicon substrate) the reflection of the probe also produces a peak in the focus result. The left image shows the result when the focus score gets calculated from the raw image. Besides the three main peaks, parasitic peaks from noisy images are produced. Figure 6.2 shows an image of such a parasitic peak.

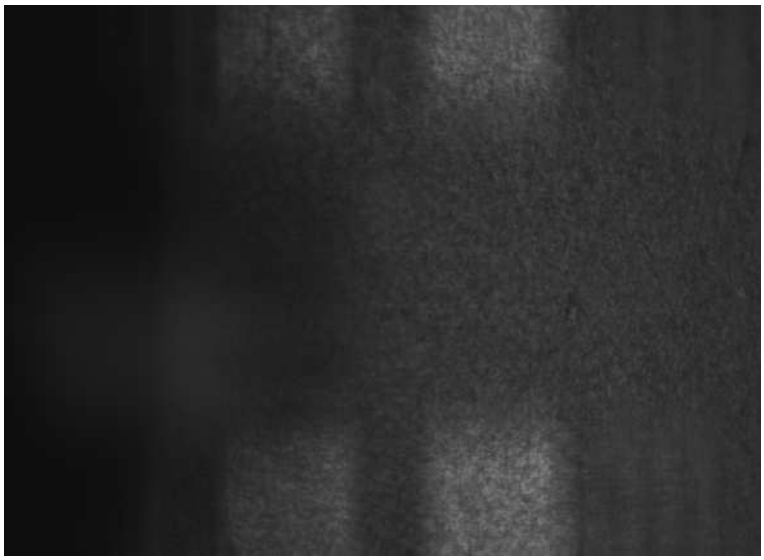

Figure 6.2: Parasitic focal plane.

To mitigate this influence, intentional gaussian blurring is done on the acquired

images. The right image in Figure 6.1 shows the result of the coarse scan, when the focus score is calculated from images which got blurred with a gaussian kernel of the size 4. Although the main peaks get smaller, the parasitic ones disappear, yet making this method more robust. Additionally, due to their bigger width, the main peaks are easier to observe. To even further increase the robustness, one can search for three equidistant peaks or average the result with a small window. The resulting peaks get a bit smaller, but due to the reduction of noise, they are easier to locate. Figure 6.3 shows the final result with the roughly determined positions of the cantilever, the sample, and the reflection of the cantilever.

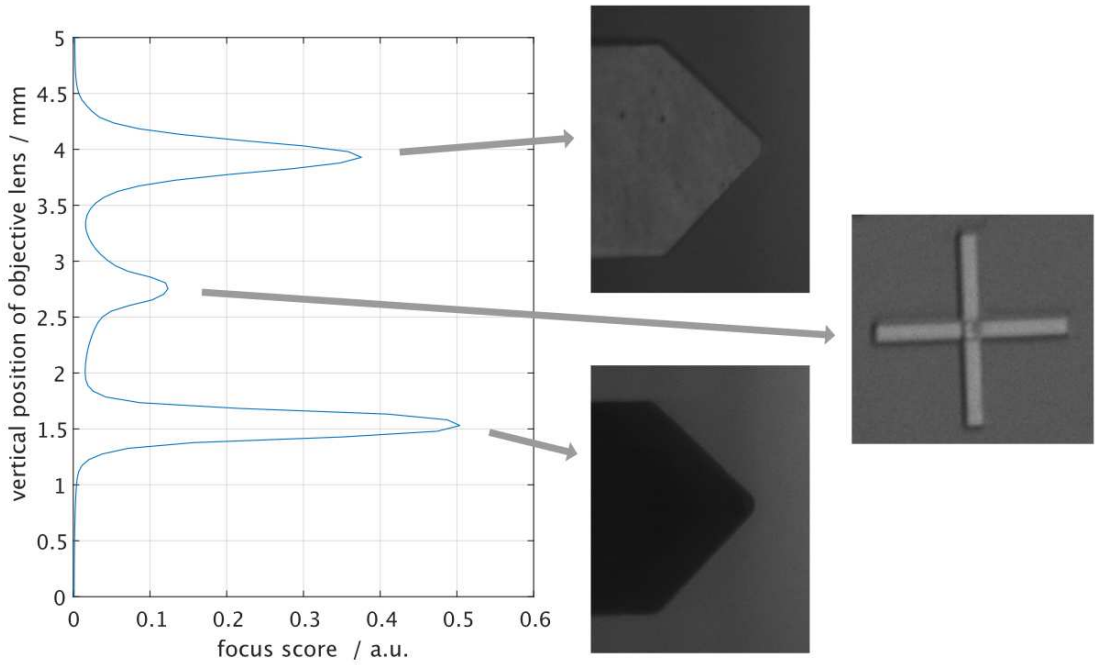


Figure 6.3: Rough scan over the whole range after post-processing. The three peaks depict the focal planes of probe, sample and probe reflection, respectively.

Now that the rough positions are known, a fine scan at higher resolution can be performed. As discussed above, the stepsize of the rough scan is 50 $\mu m$. To make the upcoming fine scan more robust, its range is adjusted to 100 $\mu m$. In order to get the best possible focus, the focusing methods are compared in the next section.

### 6.1.2 Comparison of Focusing Methods

All algorithms presented in [56] are implemented and compared to each other. A comparison of the five best performing algorithms, based on the parameters introduced in Section 4.1, are shown in Figure 6.4. The objective lens is moved 100 $\mu m$ along the roughly determined focus position of the sample. The acquired raw images are then fed to the various focus methods. The resulting focus score is recorded and normalized.

The zero-line was arbitrarily set to the maximum of the tenenbaum gradient curve. Although the methods show significantly different focus score functions, all show a maximum if the image is in focus. Deviations from from the maximum, such as the peak from the normalized variance curve, can be explained via a possible sample tilt. The uneven edge distribution on the samples surface and different weighting functions result in focus curves, where the peaks are not at the same position. This effect can be mitigated by focusing only on the ROI. As explained in Section 5.3, a marker is chosen.

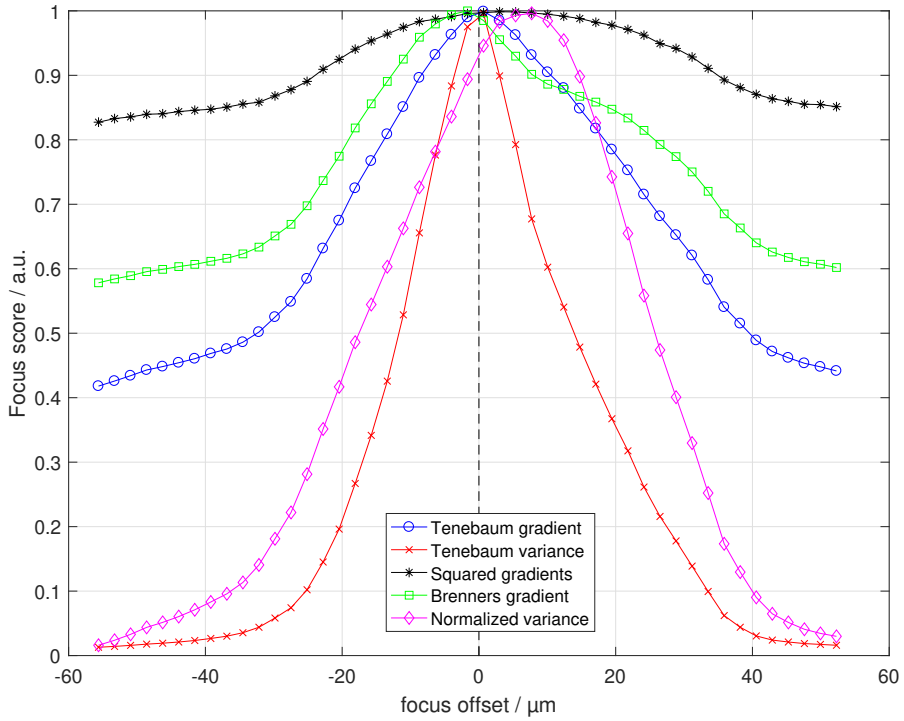


Figure 6.4: Comparison of different focusing methods.

To achieve this, a fine scan covering the whole image is performed first. Via a template matching routine, the horizontal position of the marker is then determined. The subsequent second fine scan is then performed only over a small window around this position. A 100x100 pixels window, which corresponds to a real world size of 44x44 $\mu m^2$ is chosen for this purpose. However, this window can't be chosen too small as the focusing algorithm needs some structure and edges to perform well. Figure 6.5 shows the recorded focus curves along the optical axis, when the focus algorithms are only evaluated over the small section of the image. Methods, such as "squared gradient" and "brenners gradient", are now performing much worse. Due to the less amount of edges and the relatively high noise level of the computed focus curves, the peaks almost disappear. These techniques are therefore unusable for the fine scan. However, the other methods are performing better, as they are narrower and show the peak at the same position. This can be explained by the mitigation of the influence of the possible sample tilt.

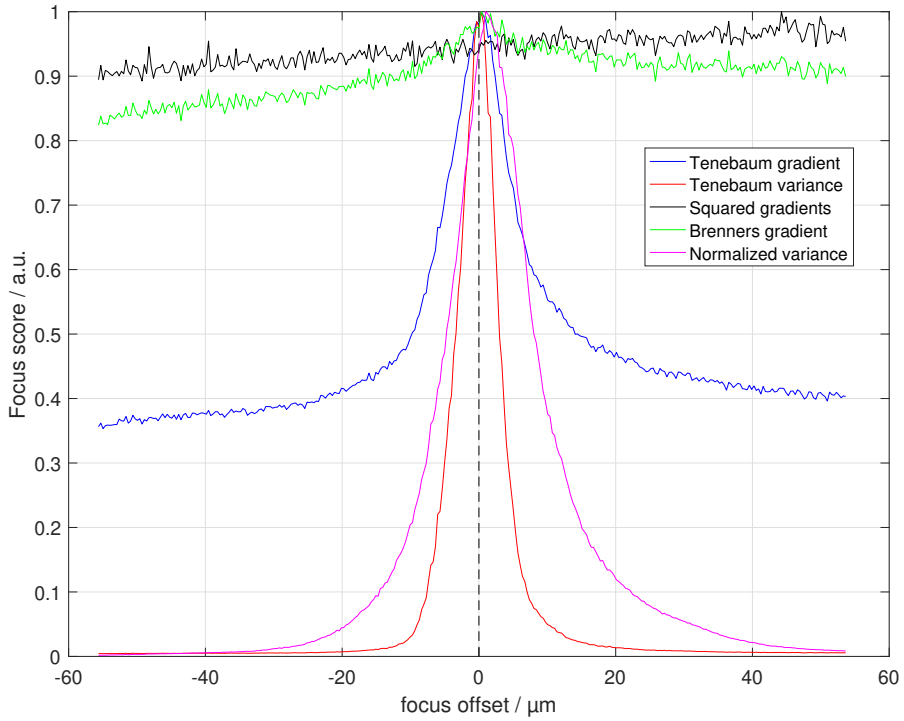


Figure 6.5: Comparison of different focusing methods on a 100x100 image patch.

Table 6.1 shows a comparison of the most important parameters from Section 4.1. As the focus curves of "squared gradient" and "brenner gradient" are too noisy, the parameter "number of false maxima" can not be determined. The execution speed is determined by calculating the focus score of several max. resolution images (2592x1944). The mean value of the computation time per image is shown.

Table 6.1: Comparison of focus algorithms.

| Method | Number of false maxima | FWHM | execution speed |
|---|---|---|---|
| Tenenbaum gradient | 0 | 22.4 $\mu m$ | 0.166 s |
| Tenenbaum variance | 0 | 5.9 $\mu m$ | 0.161 s |
| Normalized variance | 0 | 12.5 $\mu m$ | 0.243 s |
| Squared gradient | - | >100 $\mu m$ | 0.034 s |
| Brenner gradient | - | >100 $\mu m$ | 0.155 s |

It can be observed that due to its narrow peak and noiseless function, the best method for determining fine focus is the "tenenbaum variance" method. However, it is not applicable to the fast coarse scan. At a step size of 50 $\mu m/\text{image}$ it is possible that the peak gets skipped. Due to its broader peak and smooth settling around it, the "tenenbaum gradient" method is used for this purpose.

### 6.1.3 Comparison of Fast Peak Searching Algorithms

Although the framerate increases from the initial 6 FPS up to around 100 FPS (by specifying a ROI and decreasing the amount of read-out pixels), a fixed stepsize scan still requires around nine seconds:

$$time = \frac{range}{stepsize * framrate} = \frac{100\,\mu\text{m}}{113.9\,\text{nm} * 100\,\text{FPS}} = 8.77\,\text{s}\ . \tag{6.1}$$

Added to this is the time required for the focus score algorithm. The high resolution and relatively long computation time state the need for a fast peak-searching algorithm, as described in Section 4.1. Figure 6.6 shows an example of the first four iterations of the fibonacci peak search algorithm. At each iteration, 31.2% of the scanning range get excluded. With an initial range of 100 $\mu m$ and an aimed accuracy of 113.9 nm, 14 iterations are needed.

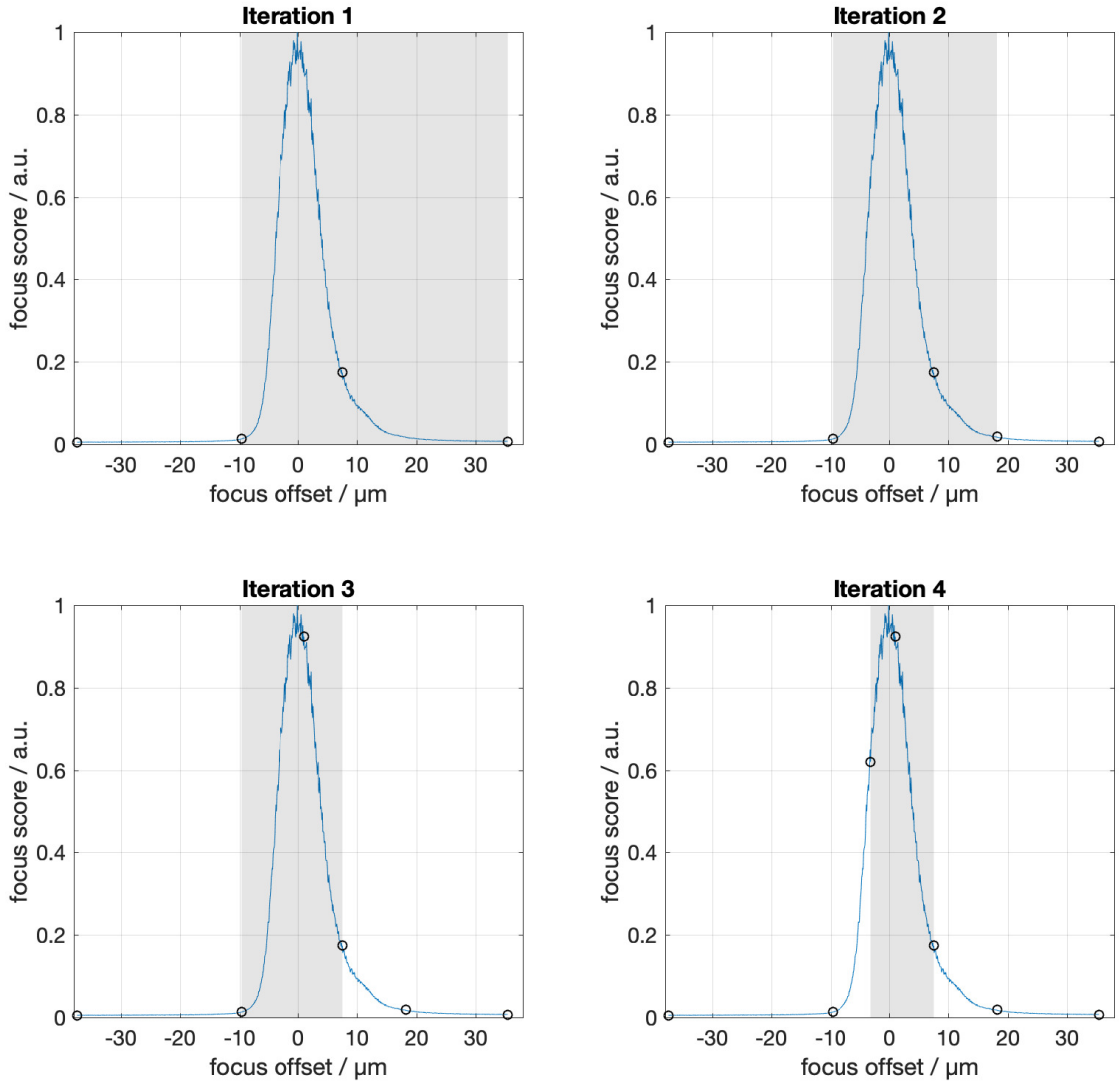


Figure 6.6: First four iterations of the fibonacci fast peak search procedure.

An iterative search is due to the high aimed accuracy impracticable. Using Equation (4.10) and adjusting $\eta$ to 7, a minimum of 43 image captions is necessary. This is much higher than the 14 iterations and 4 initial scans of the fibonacci search. The integration of a rule based procedure is only applicable to one specific focus curve. As there are several objects with different focus curves (probe, sample, reflection of probe), this method is not implemented. Additionally, the exchange of a probe would result in the need for adjusting the rule-based algorithm. Another approach is the fixed stepsize search with interpolation. Figure 6.7 shows the implemented fixed stepsize search with a gaussian interpolation. After four equidistant initial scans over the 100 $\mu m$ range, a gaussian distribution is fitted. The upcoming scan at its maximum leads to the next datapoint. By repeating this sequence of measuring at the maximum and fitting, convergence in focus position is achieved.

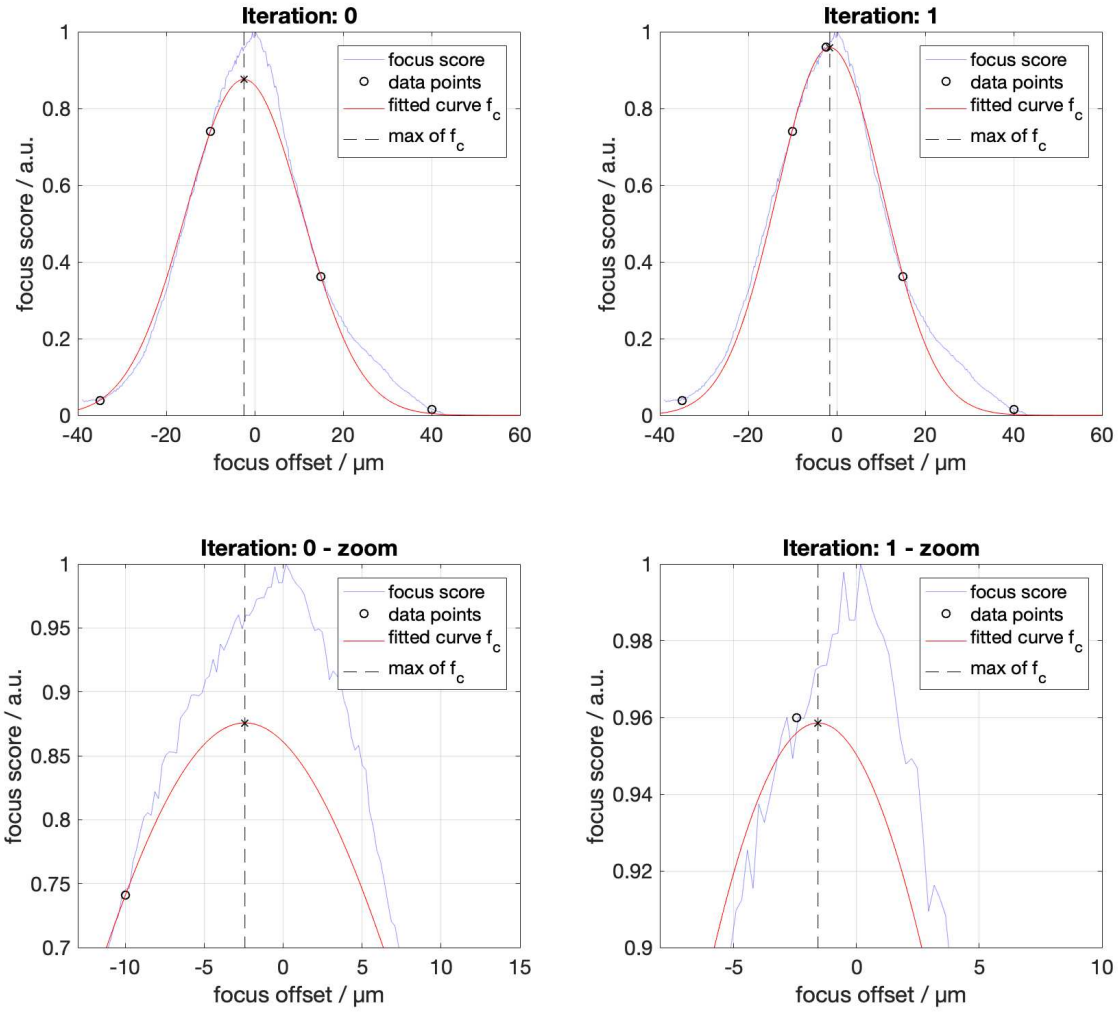


Figure 6.7: Focus procedure on the cantilever using gaussian interpolation.

The time needed for the interpolation method varies from scan to scan, as it is depending on the focus curve and the position of the four initial scans. Tests show, that a mean value of ten image captions per scan are necessary. However, due to the

computational heavy task of gaussian interpolation, the overall time is comparable to other methods, as shown in Table 6.2:

Table 6.2: Comparison of peak search algorithms.

| Method | Nr. of image captions per scan | overall time |
|---|---|---|
| Fixed stepsize search | 878 | 13.5 s |
| Fixed stepsize with interpolation | 10 | 13.8 s |
| Iterative search | 43 | 26.8 s |
| Variable stepsize/rule based search | not implemented | - |
| Fibonacci search | 14 | 12.7 s |

It turns out, that the number of image captions per scan is not the time limiting factor. Additional tasks, such as interpolation, communication with the stepper motor controller and de-/acceleration of the stepper motor have to be taken into account as well. Although the number of processed images of the fixed stepsize search is much higher, its execution time is comparable to the other methods, as the stepper motor is de-/accelerating only once. With the usage of a faster stepper motor, fast peak-search algorithms may get practicable.
The focusing procedure is then repeated for the cantilever and its reflection. As the AFM needs a tilted cantilever in order to operate, it is hard to judge which plane is in focus. To overcome this issue, the focusing algorithm is only processed over a predefined window (like the window at the sample focusing step). After the coarse scan, a template matching routine is done in order to find the tips position. Then a 150x150 window around this position is chosen to represent the ROI. This region is visualized as a white box in Figure 6.8(a). The fine scan process is then only carried out over this small window. Figure 6.8 (a) and (b) show the focused tip of the cantilever and its reflection, respectively. It can be observed, that blurring gets larger from the tip (no blurring = in focus) to the left side, due to the tilt.

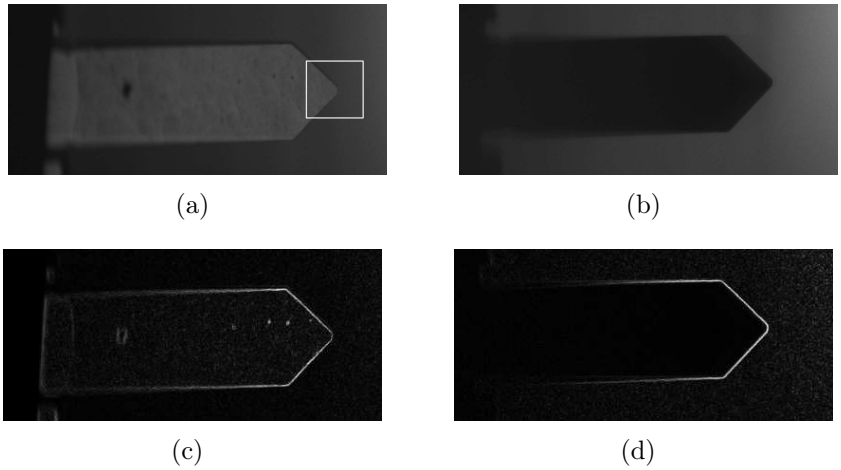

(a) (b) (c) (d)

Figure 6.8: Comparison of the normal and the reflected cantilever images / (a) and (b) depict the image of the cantilever and its reflection / (c) and (d) show their computed edge images, respectively.

Figure 6.8 (c) and (d) depict the calculated edge images using sobel operators from Section 4.1. Due to the fact, that the cantilever only gets illuminated from the top, parasitic textures only appear in the edge image of the cantilever, not in its reflection (besides the noise around the cantilever, which is equal). This results in a much wider focus curve of the cantilever (FWHM: 44 $\mu m$) than of its reflection (FWHM: 27.6 $\mu m$), as one can see in Figure 6.9. As a consequence focusing on the reflection is more accurate.

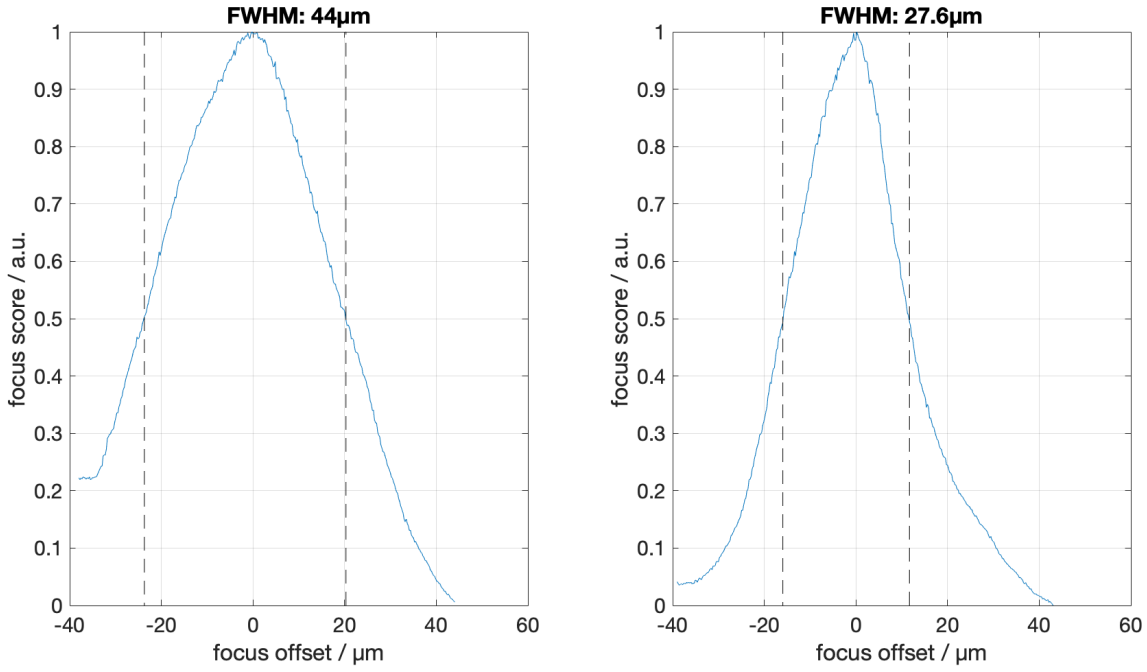


Figure 6.9: Focus curve comparison of the cantilever (left) and its reflection (right).

As there is no initial calibration between the system components, an unintentional misalignment between the Z-stage and the optical axis of the objective lens is present. This misalignment, needs to be measured in order to achieve an accurate vertical positioning and therefore reasonable results. This is accomplished, by measuring the vertical position of the cantilever ($p_{c1}$ and $p_{c2}$) at two different Z-stage positions ($p_{z1}$ and $p_{z2}$). The deviation from the measured vertical cantilever offset ($o_c = p_{c1} - p_{c2}$) to the Z-stage offset ($o_z = p_{z1} - p_{z2}$) leads to a factor $\beta$:

$$\beta = \frac{o_z}{o_c} = \frac{p_{z1} - p_{z2}}{p_{c1} - p_{c2}} \ . \tag{6.2}$$

The factor $\beta$ is then used to translate the measured probe sample offset to a positioning command for the Z-stage, in order to achieve vertical alignment.

### 6.1.4 Probe Sample Alignment Results

This section discusses the carried out measurement procedures for vertical probe sample alignment and presents the results of the evaluated positioning accuracy.

#### Measurement Procedure

The procedure for the determination of the vertical positioning accuracy is as follows:

1. Initialize the position of the cantilever and the objective lens.
2. Perform a coarse scan at lower resolution over the whole range.
3. From the three main peaks calculate the rough position of the cantilever and the sample denoted as $p_c$ and $p_s$, respectively.
4. Perform a fine scan to gain knowledge of the more accurate vertical positions and therefore the offset $o_{v1} = |p_s - p_c|$.
5. Move the cantilever towards the sample by $o_z = \frac{o_{v1}}{2}$
6. Repeat step 4, to measure the possible misalignment between the Z-stage and the optical axis and calculate the factor $\beta$.
7. Calculate the actual vertical offset $o_{v2} = o_{v1} * \beta$.
8. Move the cantilever towards the sample, till it gets deflected.
9. From the deflection signal and the Z-stage position calculate the real offset $o_{real}$

The difference between of $o_{v2}$ and $o_{real}$ is the positioning error in vertical direction.

#### Results

The above mentioned procedure was performed 200 times to get a meaningful statistic. Figure 6.10 shows the results for the vertical alignment accuracy as a histogram. Subfigure (a) depicts the measured positioning error by using the vertical position of the cantilever and the sample. Subfigure (b) shows the result by using the reflection of the cantilever and the sample. The solid red line depicts a fitted gaussian distribution, with a standard deviation of $1.07\,\mu m$ and $0.88\,\mu m$ for (a) and (b), respectively. The standard deviation is visualized as a dashed red line. Due to the absence of parasitic textures on the reflection and therefore thinner focus peak, vertical alignment is more accurate than using the position of the cantilever itself.

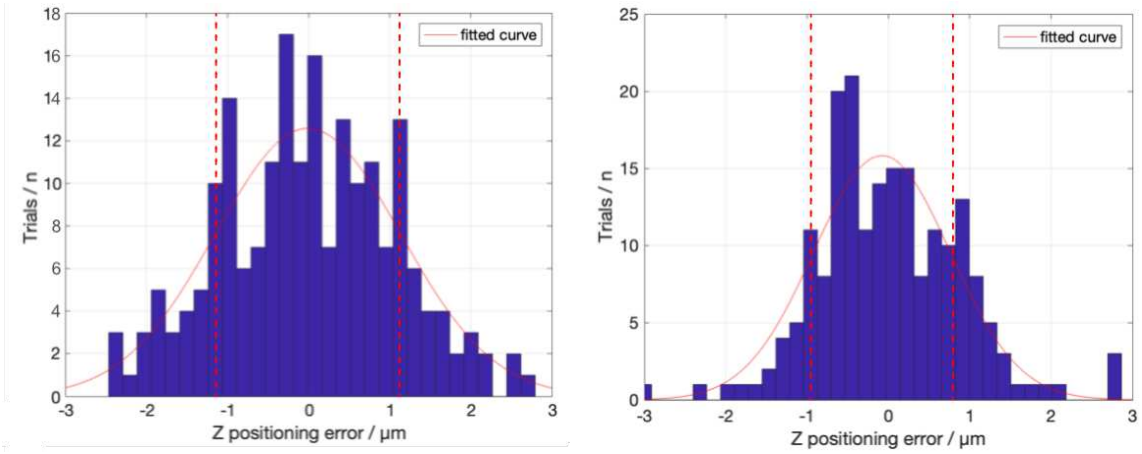


(a) (b)

Figure 6.10: Results of the vertical positioning accuracy / (a) histogram of the error, when focusing on the cantilever and the sample / (b) histogram of the error, when focusing on the reflection of the cantilever and the sample.

## 6.2 Horizontal Alignment

The vertical offset is now compensated, thus the probe and sample are in the same plane. The upcoming horizontal alignment procedure finishes the probe to sample alignment. Template matching is used to determine the x- and y-position of the marker and the cantilever in the image. However, this method is depending on the quality of the focus. Blurry images provide different template matching results, than sharp ones. Figure 6.11 shows the dependency of the template matching result on the quality of the focus.

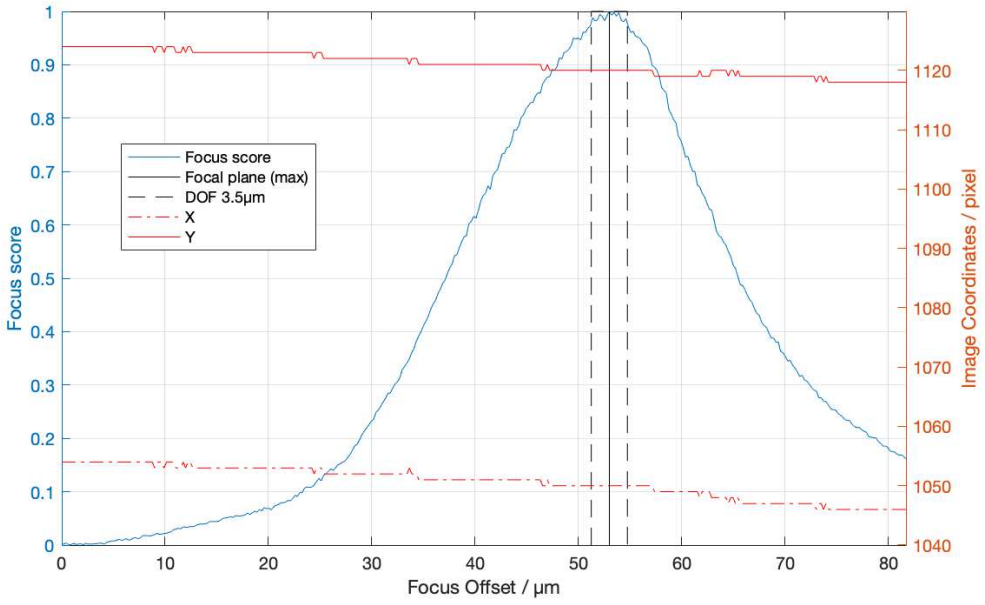


Figure 6.11: Dependency of the determined XY-position on the focus position.

The blue line shows the focus score of the cantilever over a range of 80 $\mu m$. The red lines depict the detected X- and Y-positions of the tip. As one can conclude, the position detection is fairly robust versus focus offsets. If one stays in around 10 $\mu m$ of the maximum focus score, the detected tip positions stay unchanged. If the image gets too blurry (out of focus), a shift can be observed. For a focusing accuracy of around 1 $\mu m$, this effect can be neglected.

### 6.2.1 Procedure

After the vertical alignment, the cantilever and the sample are in the same plane. Figure 6.12 show the initial state of the lateral alignment procedure.

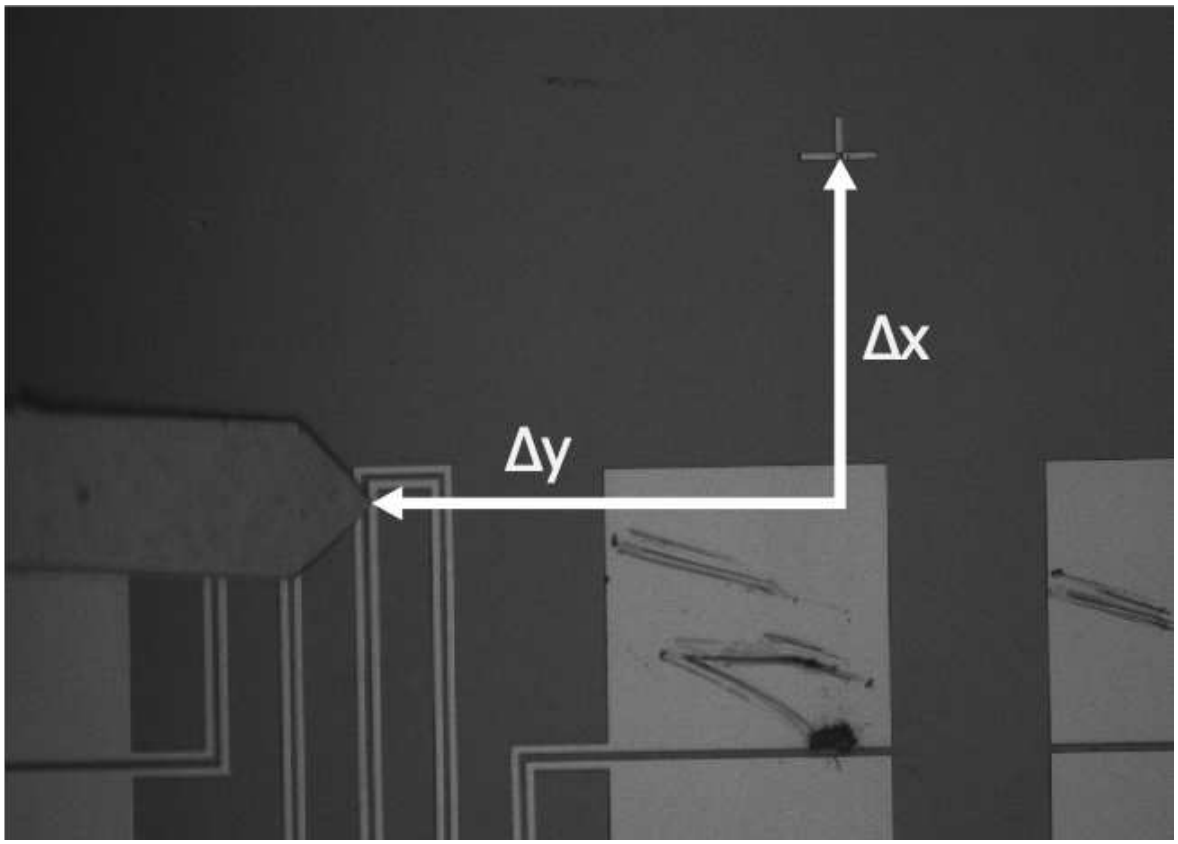


Figure 6.12: Measuring the horizontal positioning offset.

As explained in Section 5.3, a marker is used for the evaluation of the positioning accuracy, due to its small and defined structure. $\Delta x$ and $\Delta y$ depict the initial horizontal offsets from the cantilever tip to the center of the marker. These offsets need to be minimized to achieve alignment. A 150 $\mu m$ by 150 $\mu m$ contact pad can be observed in the lower section of Figure 6.12. The scratches on the pad are a result of manual alignment of a needle probe to it.

To compensate for the horizontal offset, a visual-servoing control loop is implemented. Figure 6.13 visualizes the utilized control loop structure for alignment in x direction. A second controller with the same structure is used for alignment in y direction. The underlying control loop for the stages runs at 20 kHz. The encoder measures the current position $xpi$, which is subtracted from the aimed position $xps$. The upcoming PI controller then drives the piezoelectric actuator in order to minimize $xps - xpi$. The second part of the cascaded control loop is the vision-guided loop. It runs at a frequency of 6 Hz, limited by the frame rate of the camera. The aimed position "$x\_img\_s$" and the current position "$x\_img\_i$" are the results of the template matching routine for the cantilever and the marker, respectively. The block stated as "Vision controller" then converts the calculated image offsets $\Delta x$ and $\Delta y$ into actual positioning commands for the X- and Y-stage.

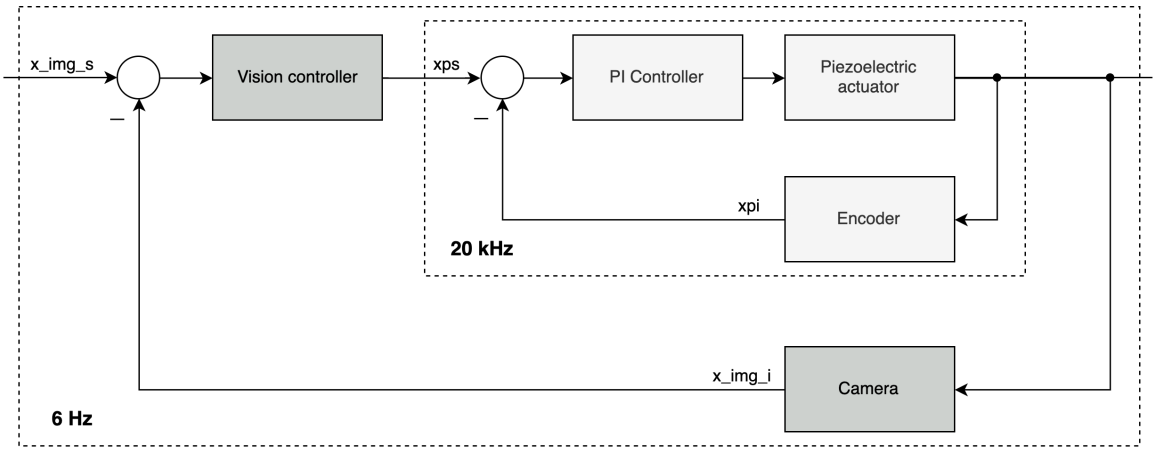


Figure 6.13: Control scheme for lateral alignment.

After running a template matching routine for the cantilever and the marker, their x- and y- positions are known. The difference leads to the horizontal offset in image coordinates: $\Delta x_{image} = x_{cant} - x_{marker}$ and $\Delta y_{image} = y_{cant} - y_{marker}$. The positioning command for the X- and Y-stage can then be calculated, using Equation (6.3):

$$\begin{bmatrix} \Delta x_{stage} \\ \Delta y_{stage} \end{bmatrix} = \begin{bmatrix} \Delta x_{image} \\ \Delta y_{image} \end{bmatrix} * 440\,{}^{\mathrm{nm}}/_{\mathrm{Pixel}} * \frac{1}{50}\,{}^{\mathrm{steps}}/_{\mathrm{nm}} = \begin{bmatrix} \Delta x_{image} \\ \Delta y_{image} \end{bmatrix} * 8.8\,{}^{\mathrm{steps}}/_{\mathrm{Pixel}}\,. \quad (6.3)$$

After adjusting the position of the stages with the calculated offsets $\begin{bmatrix} \Delta x_{stage} \\ \Delta y_{stage} \end{bmatrix}$ one receives an alignment as shown in Figure 6.14. This is a result of the unknown misalignment between the X- and Y-stage to the camera frame. To account for this, the misalignment is modelled [75].

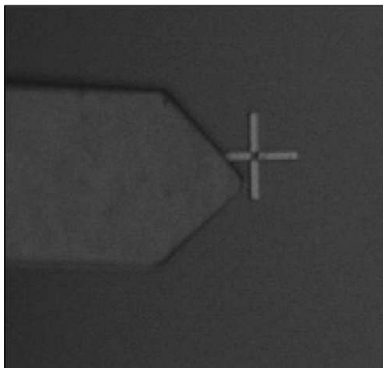

Figure 6.14: Misalignment after first iteration.

Let $x_{pi}$ and $y_{pi}$ be the pixel coordinates of the marker at the initial state (i=1) and after the first alignment step (i=2). $x_{si}$ and $y_{si}$ are the corresponding positions of the X- and Y-stage. After linearisation one receives a block of formulas:

$$\begin{aligned} a * x_{p1} + b * y_{p1} &= x_{s1} \\ c * x_{p1} + d * y_{p1} &= y_{s1} \\ a * x_{p2} + b * y_{p2} &= x_{s2} \\ c * x_{p2} + d * y_{p2} &= y_{s2} \end{aligned}$$

which can be rewritten as

$$\begin{bmatrix} x_{p1} & y_{p1} \\ x_{p2} & y_{p2} \end{bmatrix} \begin{bmatrix} a & c \\ b & d \end{bmatrix} = \begin{bmatrix} x_{s1} & y_{s1} \\ x_{s2} & y_{s2} \end{bmatrix} \quad \widehat{=} \quad AZ = B \tag{6.4}$$

The modelled misalignment is the characteristic matrix Z, which can be calculated using Equation (6.5).

$$Z = A^{-1}B \tag{6.5}$$

Z is then used in the next step to correct for the misalignment. $\begin{bmatrix} x_{p3} & y_{p3} \end{bmatrix}$ are the aimed positions of the marker (= position of the cantilevers tip). The corresponding stage commands are calculated as follows:

$$\begin{bmatrix} x_{p3} & y_{p3} \end{bmatrix} \begin{bmatrix} a & c \\ b & d \end{bmatrix} = \begin{bmatrix} x_{s3} & y_{s3} \end{bmatrix} \tag{6.6}$$

In order to check the markers position, the cantilever has to be moved out of the focal plane. Figure 6.15 visualizes this step, where the silhouette of the cantilever can still be roughly observed.

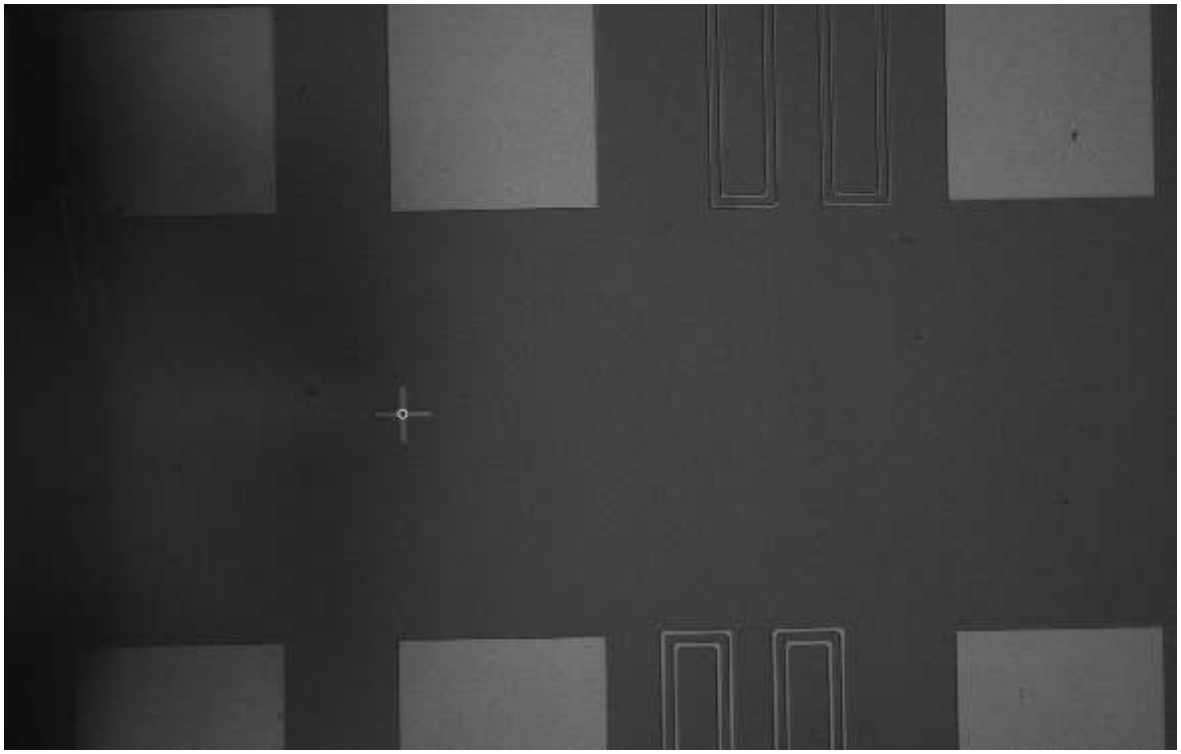

Figure 6.15: Final position of the marker after compensating for misalignment.

The white circle depicts the aimed position. The control loop is executed, till the measured horizontal offsets $\Delta x$ and $\Delta y$ are zero. An average number of iterations of 2-3 is necessary, which results in an overall duration for the horizontal alignment of around four seconds. After moving the cantilever back to the surface of the sample, one receives a final alignment like in Figure 6.16. As explained on the SEM image of the cantilever in Section 5.2.5, there exists a small offset from the detected tip, to the actual AFM tip. Due to the fact, that this offset is taken into account, the marker is covered by the cantilever.

The alignment is now finished. The upcoming step is the evaluation of the positioning error in horizontal direction. This step is done via an AFM scan. The detailed procedure and Matlab/SIMULINK implementation can be found in Appendix A.

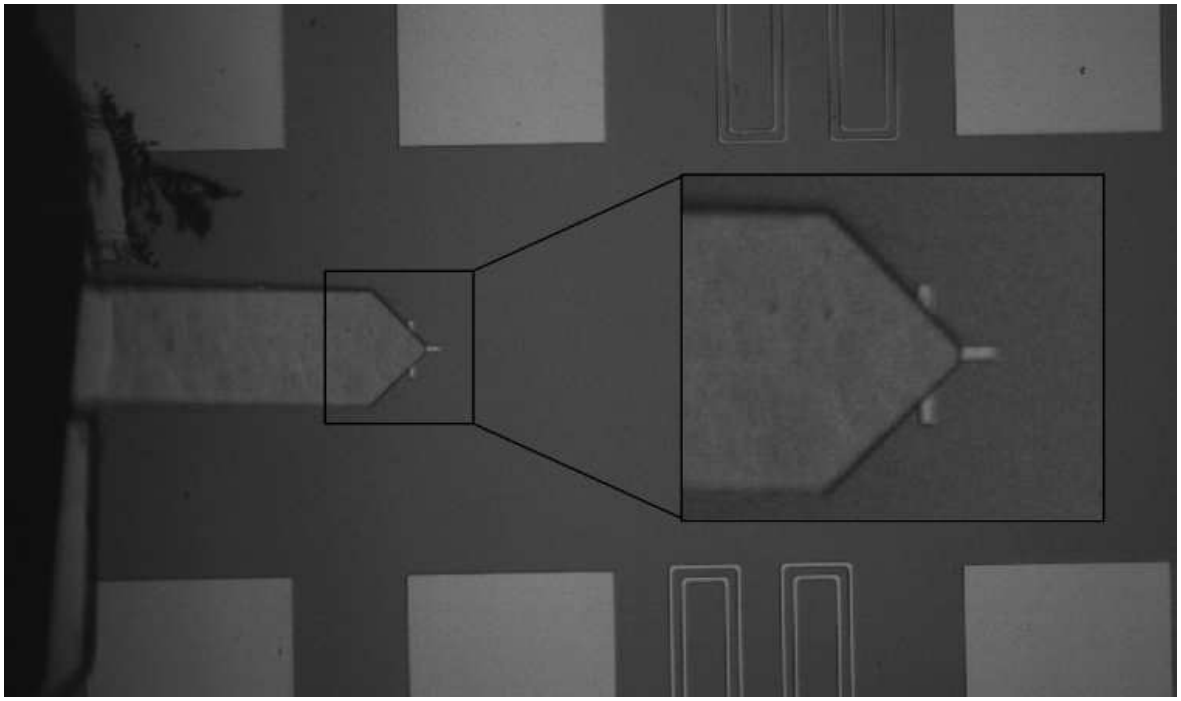

Figure 6.16: Final alignment of the probe (= cantilever) to the sample (=marker).

### 6.2.2 Probe Sample Alignment Results

This section discusses the carried out measurements to evaluate the positioning accuracy in horizontal direction. Two different camera resolutions are used, in order to investigate their influence.

#### High Resolution / 2592x1944

By using the maximum resolution of the camera (2592x1944) and above described procedure, alignment was carried out. 28 trials with a random initialization were done to achieve a meaningful statistic. Figure 6.17(a) shows one example of an AFM image after the alignment procedure. To evaluate the horizontal positioning error, a specific reference position needs to be established. The center of the marker was chosen. From the AFM image, an edge image is computed using canny edge detector. Via the computation of the hough transformation [76] of the edge image, lines are fitted. The four most pronounced peaks depict the sidewalls of the marker. The mean value of the four lines, lead to the center of the marker. The deviation of this center to the middle of the acquired AFM image is then determined as the horizontal positioning offset. Figure 6.17(b) and 6.17(c) show the hough transformation and the edge image with fitted lines, respectively. Figure 6.17(d) depicts the horizontal positioning offset for all 30 trials.

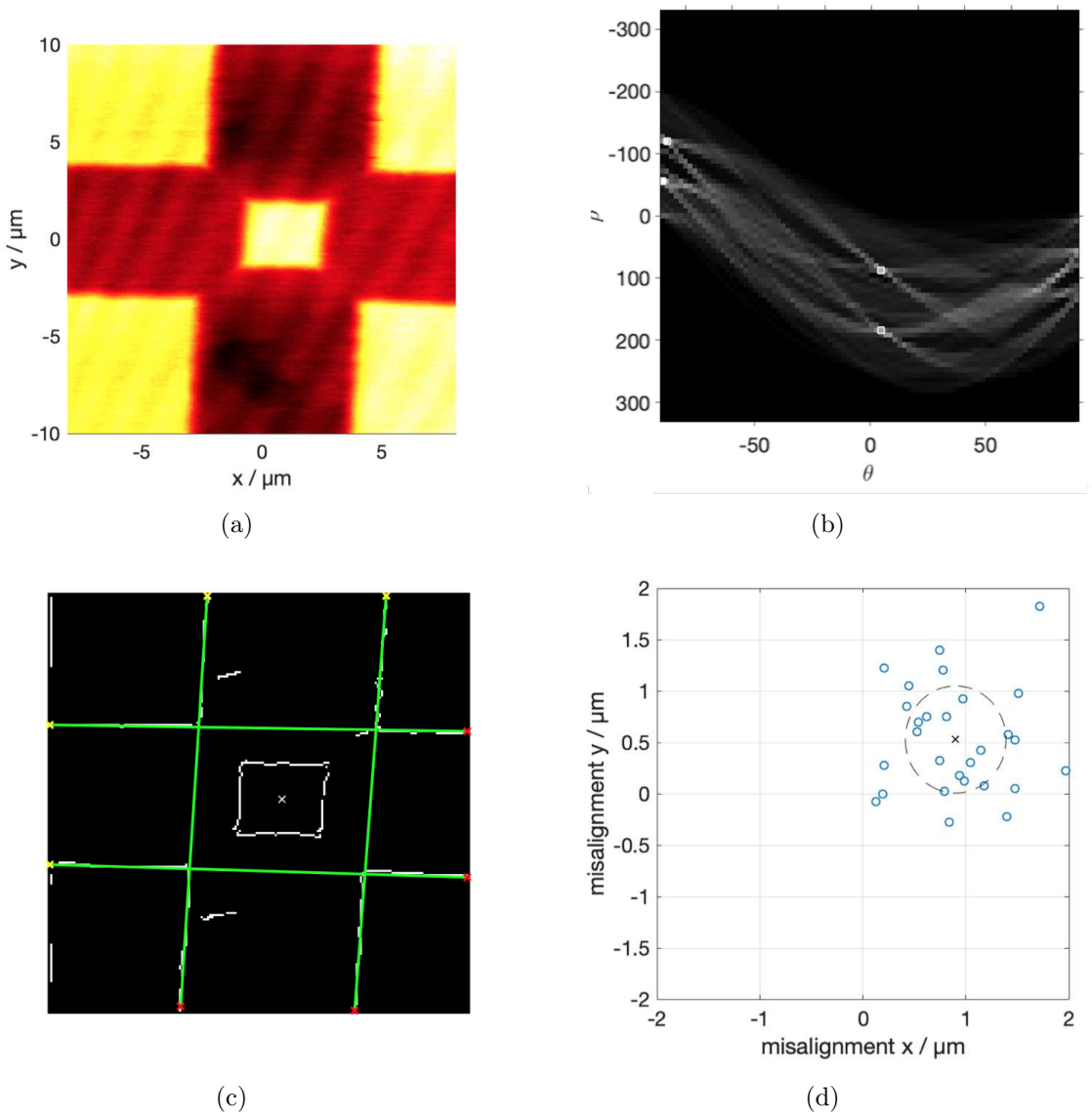


Figure 6.17: Measurement result using the highest resolution (2592x1944) / (a) shows the plane fitted AFM image / (b) depicts the hough transformed edge image with the four biggest peaks / (c) shows the edge image of (a) and the four fitted lines and a cross at the center of the marker / (d) shows the final results of the measurement series (n=30) with their alignment errors.

The black dashed ellipse in Figure 6.17(d) visualizes a fitted gaussian distribution. Its radius is the standard deviation of the positioning error in x and y direction, which is 0.49 $\mu m$ and 0.52 $\mu m$, respectively. This observation correlates with the RWPS of 0.44 $\mu m$, which can be calculated using Equation (5.4).

### Low Resolution / 648x484

To further investigate the influence of the RWPS on the positioning accuracy, the resolution of the camera is scaled down to 648x484, while maintaining the maximum

FOV. Figures 6.18(a)-(d) show the results for the same evaluation procedure as described in the previous section.

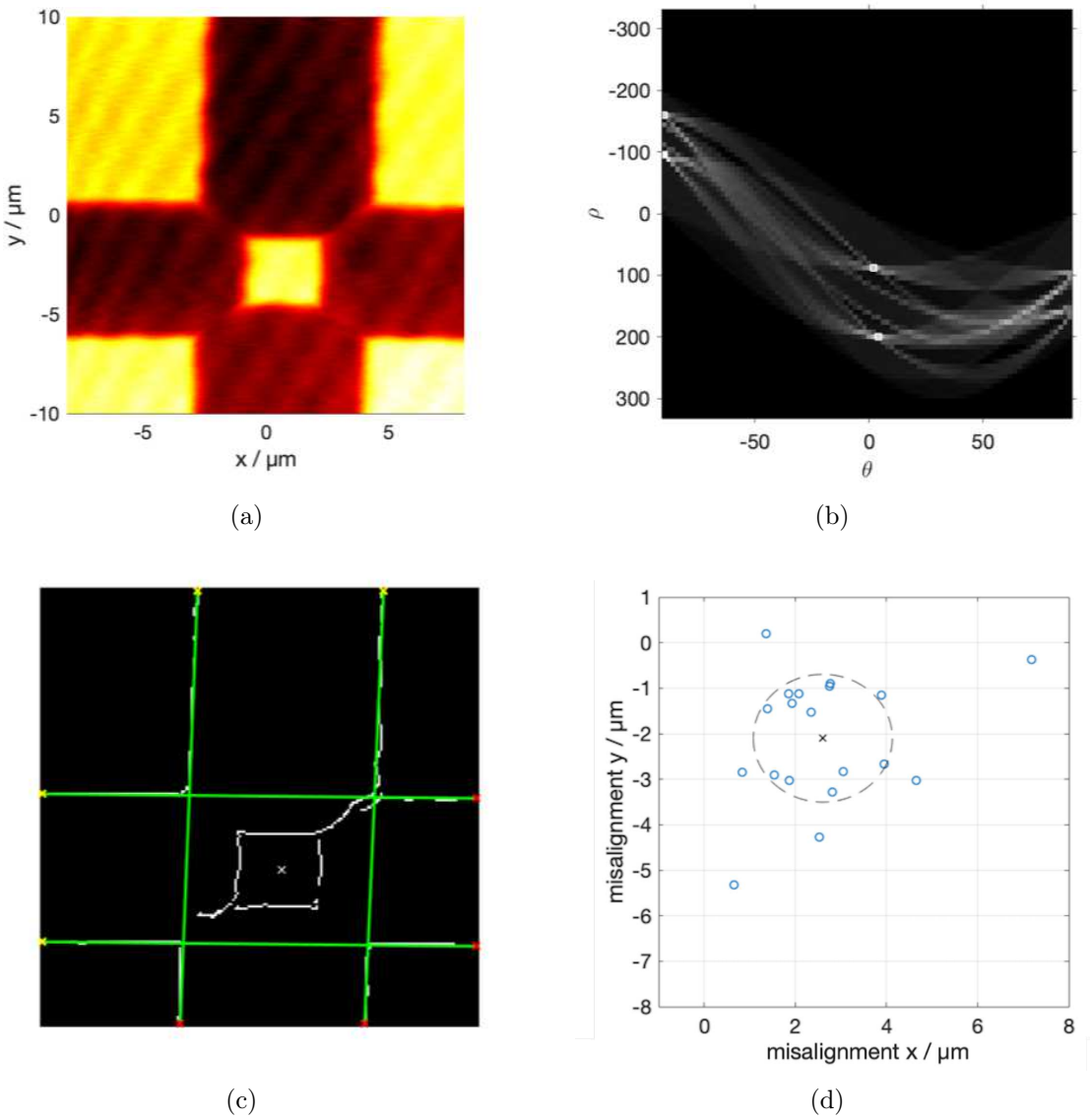


(a) (b)

(c) (d)

Figure 6.18: Measurement result using a lower resolution (648x484) / (a) shows the plane fitted AFM image / (b) depicts the hough transformed edge image with the four biggest peaks / (c) shows the edge image of (a) and the four fitted lines and a cross at the center of the marker / (d) shows the final results of the measurement series (n=20) with their alignment errors.

The radius of the fitted gaussian distribution ellipse is 1.52 $\mu m$ and 1.4 $\mu m$ in x and y direction, respectively. This is again in correlation with the RWPS, which is calculated as 1.76 $\mu m$.
To summarize this chapter, the aimed probe sample alignment accuracy in the micrometer range is achieved in vertical as well as in horizontal direction. Limits, regarding positioning accuracy and execution speed, are presented based on the system parameters.

# CHAPTER 7

# Summary, Conclusion and Outlook

In this thesis, an automated vision-guided probe sample alignment system was successfully designed and built. The results regarding positioning accuracy are summarized in this chapter. An outlook on possible future work to achieve further developments is given.

## 7.1 Summary and Conclusion

The development in the field of integrated circuits, as well as a trend towards higher frequencies leads to ever growing circuit densities on-chip and thereby smaller contact pads. However, proper alignment between the signal-feeding probe to the contact pad is necessary to maintain the signal integrity throughout the measurement and testing of these circuits. Due to the small contact pad sizes and limited alignment accuracy, contact impedances may change in an indeterminable way, thus resulting in bad measurement results. More precise probe to sample alignments are therefore necessary, to ensure reproducible and meaningful measurement data.
The fulfilment of similar requirements in other scientific fields, such as biology or micromechanics, has already been sought with the implementation of an automated vision-guided approach. This approach has been adapted to automate the probe sample alignment process. Via observation with a camera and the integration of various machine-vision techniques, the spatial position of the probe and the sample are recorded. Positioning stages are then used for the alignment, which is based on the measured positions. As the evaluation of the alignment accuracy is a main part of this work, a piezoresistive cantilever probe and a separate evaluation stage are used. This results in the ability of performing an AFM scan after finished alignment, thus determining the spatial offset.

Several focus methods and fast-peak searching algorithms were presented and compared to each other. The methods "Tenenbaum gradient and variance" are chosen

for the focus detection procedure, as they have the best performance based on parameters, such as global/local accuracy, execution speed and robustness against noise. Template matching is used for the determination of the horizontal position of the objects.
Due to timing and stepsize reasons, a coarse focus scan using the method "Tenenbaum gradient" is performed first. The subsequent fine scan, using a fast-peak searching algorithm and the method Tenenbaum variance", yields the vertical position of the cantilever and the sample. After that, vertical alignment is carried out and its positioning error is evaluated, as shown in Table 7.1:

Table 7.1: Vertical alignment accuracy.

| Focusing on | Trials | $\sigma$ of positioning error |
|---|---|---|
| Cantilever / Sample | 200 | $1.07\,\mu m$ |
| Reflection of cantilever / Sample | 200 | $0.88\,\mu m$ |

Measurement of the cantilevers vertical position can be achieved, either by focusing on itself, or by focusing on its reflection. As discussed in Section 6.1.3, the cantilever is only illuminated from the top. This results in the absence of parasitic structures on the reflection, which narrows the focus curve and improves the focusing accuracy. Therefore, a better vertical positioning accuracy is achieved, by focusing on the reflection of the cantilever. The limiting factor of the vertical alignment is the objective lens DOF. However, this parameter can not be chosen too small, as it is directly related to a larger opening angle $\Theta$ and therefore a smaller working distance. This would require the development of a more compact probe alignment setup. A trade-off between vertical alignment accuracy and ease of use is the result.

The next part of this thesis deals with the evaluation of the horizontal alignment accuracy. Conventional markers are used as test structures for the procedure, as they incorporate small dimensions and reference points can be easily determined for evaluating the positioning accuracy. Continuous detection of the horizontal positioning offset from the probes tip to the center of the marker is achieved via template matching. By controlling the alignment stages, horizontal alignment accuracy as shown in Table 7.2 is achieved:

Table 7.2: Horizontal alignment accuracy.

| Camera resolution | Real world pixel size (RWPS) | Trials | $\sigma$ of positioning error: x / y |
|---|---|---|---|
| 2592x1944 | $0.44\,\mu m$ | 30 | $0.49\,\mu m$ / $0.52\,\mu m$ |
| 648x484 | $1.76\,\mu m$ | 20 | $1.52\,\mu m$ / $1.40\,\mu m$ |

Results show a connection between the RWPS parameter of the optical system and the measured standard deviation $\sigma$ of the horizontal positioning error. This is a result of the template matching method, as it provides the position of an object down to one pixel. This limiting factor can be enhanced, either by increasing the camera resolution while maintaining or even decreasing the sensor size, or by increasing the magnification of the

optical system. However, greater resolution or smaller sensor size results in a smaller pixel size ($pixel\ size = {}^{sensor\ size}/_{camera\ resolution}$). Besides manufacturing techniques, which limit the achievable pixel size, more illumination is necessary for smaller pixels. Additionally, as more pixels need to be read-out, the frame rate will decrease, leading to slower alignment procedures. Similar to the vertical alignment, greater magnification will also enhance the accuracy. However, the corresponding lower working distance will again limit the freedom of vertical movement. A trade-off between horizontal/vertical positioning accuracy and alignment speed is the result.

The implementation of an automated vision-guided alignment, results in the advantage that no perfect calibration between the system components is needed. Deviations from the XY-stage axes to the camera frame axes and the Z-stage axis to the optical axis can easily be counteracted. The therefore needed additional measurements take some time, but are only done once, as the components maintain their initial orientation. Table 7.3 shows a list of the duration of each step of the alignment procedure:

Table 7.3: Average time needed for probe sample alignment.

| Task | Duration |
|---|---|
| Coarse focus scan | 4 s |
| Fine focus scan / sample | 13 s |
| Fine focus scan / cantilever | 13 s |
| Movement of cantilever | 0.5 s |
| Fine focus scan 2 / cantilever | 13 s |
| Vertical alignment | 0.5 s |
| Template matching / horizontal position detection | 1 s |
| Several iterations for horizontal alignment | 3 s |
| Overall alignment duration | 48 s |

It is shown that the majority of the overall time is claimed by the vertical position detection process (fine focus). As concluded in Section 6.1.3, the stepper motor with its controller board and the computation heavy task of focus detection are the time limiting factors. By increasing the velocity and de/-acceleration of the stepper motor, faster focusing can be achieved.

To conclude this thesis an automated vision-guided probe sample alignment system was designed and implemented. An evaluation system was developed to measure the positioning accuracy. The overall targeted probe sample alignment accuracy in the micrometer range was achieved and limiting factors were derived.

## 7.2 Outlook

To further increase the system performance, regarding alignment accuracy and speed, several points need to be considered. The development of a more compact probe alignment setup leads to the ability of integrating an objective lens with a smaller working distance. The resulting smaller DOF and higher magnification will not only enhance the focusing accuracy, but also the horizontal positioning accuracy. Furthermore, future work may focus on the integration of more than one probe, as it is usually used in probing stations. The larger amount of probes states the need for faster focusing procedures. As the stepper motor is the time-limiting factor for the vertical alignment, it is proposed to develop and integrate algorithms, which dynamically adjust the micro-step mode of the stepper motor controller. Higher speeds for non-resolution dependent steps can be achieved. In addition to evaluating the spatial offset, the measurement of the rotational error can also be implemented in future work. For this task, the development of a more complex alignment-stage setup is needed.

# Bibliography


[1] G. E. Moore, "Progress in digital integrated electronics [technical literaiture, copyright 1975 ieee. reprinted, with permission. technical digest. international electron devices meeting, ieee, 1975, pp. 11-13.]," *IEEE Solid-State Circuits Society Newsletter*, vol. 11, no. 3, pp. 36–37, Sep. 2006.

[2] W. M. Holt, "1.1 moore's law: A path going forward," in *2016 IEEE International Solid-State Circuits Conference (ISSCC)*, Jan 2016, pp. 8–13.

[3] R. Kapoor and R. Adner, "Technology interdependence and the evolution of semiconductor lithography," *Solid State Technology*, vol. 50, pp. 51–54, 11 2007.

[4] W. M. Arden, "The international technology roadmap for semiconductors-perspectives and challenges for the next 15 years," *Current Opinion in Solid State and Materials Science*, vol. 6, no. 5, pp. 371 – 377, 2002.

[5] F. Rahman, D. Forte, and M. M. Tehranipoor, "Reliability vs. security: Challenges and opportunities for developing reliable and secure integrated circuits," in *2016 IEEE International Reliability Physics Symposium (IRPS)*, April 2016, pp. 4C–6–1–4C–6–10.

[6] K. Wu, "Towards the development of terahertz substrate integrated circuit technology," in *2010 Topical Meeting on Silicon Monolithic Integrated Circuits in RF Systems (SiRF)*, Jan 2010, pp. 116–119.

[7] W. R. Deal, K. Leong, V. Radisic, S. Sarkozy, B. Gorospe, J. Lee, P. H. Liu, W. Yoshida, J. Zhou, M. Lange, R. Lai, and X. B. Mei, "Low noise amplification at 0.67 thz using 30 nm inp hemts," *IEEE Microwave and Wireless Components Letters*, vol. 21, no. 7, pp. 368–370, July 2011.

[8] C. Doan, "Introduction to on-wafer characterization at microwave frequencies," Dec. 2017.

[9] F. von Kleist-Retzow, T. Tiemerding, P. Elfert, and O. Haenssler, "Automated calibration of rf on-wafer probing and evaluation of probe misalignment effects

using a desktop micro-factory," *Journal of Computer and Communications*, vol. 04, pp. 61–67, 01 2016.

[10] F. T. von Kleist-Retzow, O. C. Haenssler, and S. Fatikow, "Simulation of probe misalignment effects during rf on-wafer probing," in *2016 41st International Conference on Infrared, Millimeter, and Terahertz waves (IRMMW-THz)*, Sep. 2016, pp. 1–2.

[11] B. Tamadazte, N. L. Piat, and E. Marchand, "A direct visual servoing scheme for automatic nanopositioning," *IEEE/ASME Transactions on Mechatronics*, vol. 17, no. 4, pp. 728–736, Aug 2012.

[12] *On-Wafer Vector Network Analyzer Calibration and Measurements*, Cascade Microtech Inc, application Note.

[13] Mpi ts3000 probe station. [Online]. Available: https://www.mpi-corporation.com/ast/engineering-probe-systems/mpi-automated-systems/ts3000-probe-system/

[14] Manual probe station alignment. [Online]. Available: https://departments.icmab.es/nanopto/probe-station-thermal-and-electrical-conductivity-measurements/

[15] Manual probe station. [Online]. Available: https://www.formfactor.com/product/probe-systems/150-mm-systems/mps150/

[16] E. J. Marinissen, D. Y. Lee, J. P. Hayes, C. Sellathamby, B. Moore, S. Slupsky, and L. Pujol, "Contactless testing: Possibility or pipe-dream?" in *Proceedings of the Conference on Design, Automation and Test in Europe*. 3001 Leuven, Belgium, Belgium: European Design and Automation Association, 2009, pp. 676–681.

[17] C. Wu, C. Huang, S. Huang, P. Huang, T. Chang, and Y. Hsing, "The hoy tester-can ic testing go wireless?" in *2006 International Symposium on VLSI Design, Automation and Test*, April 2006, pp. 1–4.

[18] C. V. Sellathamby, M. M. Reja, Lin Fu, B. Bai, E. Reid, S. H. Slupsky, I. M. Filanovsky, and K. Iniewski, "Noncontact wafer probe using wireless probe cards," in *IEEE International Conference on Test, 2005.*, Nov 2005, pp. 6 pp.–452.

[19] D. Y. Lee, D. D. Wentzloff, and J. P. Hayes, "Wireless wafer-level testing of integrated circuits via capacitively-coupled channels," in *14th IEEE International Symposium on Design and Diagnostics of Electronic Circuits and Systems*, April 2011, pp. 99–104.

[20] G. Kim, M. Takamiya, and T. Sakurai, "A capacitive coupling interface with high sensitivity for wireless wafer testing," in *2009 IEEE International Conference on 3D System Integration*, Sep. 2009, pp. 1–5.

[21] M. Urteaga, Z. Griffith, M. Seo, J. Hacker, and M. J. W. Rodwell, "Inp hbt technologies for thz integrated circuits," *Proceedings of the IEEE*, vol. 105, no. 6, pp. 1051–1067, June 2017.

[22] L. Chen, C. Zhang, T. J. Reck, C. Groppil, A. Arsenovic, A. Lichtenberger, R. M. Weikle, and N. S. Barker, "Terahertz micromachined on-wafer probes: Repeatability and robustness," in *2011 IEEE MTT-S International Microwave Symposium*, June 2011, pp. 1–4.

[23] M. F. Bauwens, N. Alijabbari, A. W. Lichtenberger, N. S. Barker, and R. M. Weikle, "A 1.1 thz micromachined on-wafer probe," in *2014 IEEE MTT-S International Microwave Symposium (IMS2014)*, June 2014, pp. 1–4.

[24] T. J. Reck, L. Chen, C. Zhang, A. Arsenovic, C. Groppi, A. Lichtenberger, R. M. Weikle, and N. S. Barker, "Micromachined probes for submillimeter-wave on-wafer measurements-part ii: Rf design and characterization," *IEEE Transactions on Terahertz Science and Technology*, vol. 1, no. 2, pp. 357–363, Nov 2011.

[25] A. Safwat and L. A. Hayden, "Sensitivity analysis of calibration standards for fixed probe spacing on-wafer calibration techniques [vector network analyzers]," *2002 IEEE MTT-S International Microwave Symposium Digest (Cat. No.02CH37278)*, vol. 3, pp. 2257–2260 vol.3, 2002.

[26] A. P. Davidson, E. Strid, and K. Jones, "Achieving greater on-wafer s-parameter accuracy with the lrm calibration technique," *34th ARFTG Conference Digest*, vol. 16, pp. 61–66, 1989.

[27] S. Padmanabhan, P. Kirby, J. Daniel, and L. Dunleavy, "Accurate broadband on-wafer solt calibrations with complex load and thru models," in *61st ARFTG Conference Digest, Spring 2003.*, June 2003, pp. 5–10.

[28] W. Zhiming, H. Hui, H. Zhifu, Z. Zhuobin, X. Wang, L. Xiaobin, L. Jun, Y. Songyuan, and L. Xin, "Comparison of on-wafer calibrations for thz inp-based phemts applications," *Journal of Semiconductors*, vol. 36, 06 2015.

[29] G. Tang, H. Yao, X. Ma, Z. Jin, and X. Liu, "On-wafer de-embedding techniques from 0.1 to 110 GHz," *Journal of Semiconductors*, vol. 36, no. 5, p. 054012, may 2015.

[30] E. P. Vandamme, D. M. M. . Schreurs, and G. Van Dinther, "Improved three-step de-embedding method to accurately account for the influence of pad parasitics in silicon on-wafer rf test-structures," *IEEE Transactions on Electron Devices*, vol. 48, no. 4, pp. 737–742, April 2001.

[31] K. Daffe, G. Dambrine, F. von Kleist-Retzow, and K. Haddadi, "Rf wafer probing with improved contact repeatability using nanometer positioning," in *2016 87th ARFTG Microwave Measurement Conference (ARFTG)*, May 2016, pp. 1–4.

[32] R. Sakamaki and M. Horibe, "Accuracy improvement of on-wafer measurement at millimeter-wave frequency by a full-automatic rf probe-tip alignment technique," in *2018 91st ARFTG Microwave Measurement Conference (ARFTG)*, June 2018, pp. 1–4.

[33] R. Sakamaki and M. Horibe, "Realization of accurate on-wafer measurement using precision probing technique at millimeter-wave frequency," *IEEE Transactions on Instrumentation and Measurement*, vol. 67, no. 8, pp. 1940–1945, Aug 2018.

[34] J. Laskar, J. J. Bautista, M. Nishimoto, M. Hamai, and R. Lai, "Development of accurate on-wafer, cryogenic characterization techniques," *IEEE Transactions on Microwave Theory and Techniques*, vol. 44, no. 7, pp. 1178–1183, July 1996.

[35] D. Russell, K. Cleary, and R. Reeves, "Cryogenic probe station for on-wafer characterization of electrical devices," *Review of Scientific Instruments*, vol. 83, no. 4, p. 044703, 2012.

[36] V. M. Hietala, M. S. Housel, and R. B. Caldwell, "Network analyzer calibration for cryogenic on-wafer measurements," in *43rd ARFTG Conference Digest*, vol. 25, May 1994, pp. 24–33.

[37] X. Liu, R. Fernandes, M. Gertsenstein, A. Perumalsamy, I. Lai, M. Chi, K. H. Moley, E. Greenblatt, I. Jurisica, R. F. Casper, Y. Sun, and A. Jurisicova, "Automated microinjection of recombinant bcl-x into mouse zygotes enhances embryo development," *PLOS ONE*, vol. 6, no. 7, pp. 1–10, 07 2011.

[38] H. Wang, K. Bai, J. Cui, Q. Shi, T. Sun, Q. Huang, P. Dario, and T. Fukuda, "Three-dimensional autofocusing visual feedback for automated rare cells sorting in fluorescence microscopy," *Micromachines*, vol. 10, p. 567, 08 2019.

[39] P. Ouyang, W. Zhang, M. M. Gupta, and W. Zhao, "Overview of the development of a visual based automated bio-micromanipulation system," *Mechatronics*, vol. 17, no. 10, pp. 578 – 588, 2007.

[40] H.-S. Choi, D.-C. Lee, S.-S. Kim, and C.-S. Han, "The development of a microgripper with a perturbation-based configuration design method," *Journal of Micromechanics and Microengineering*, vol. 15, no. 6, pp. 1327–1333, may 2005.

[41] N. Chronis and L. P. Lee, "Electrothermally activated su-8 microgripper for single cell manipulation in solution," *Journal of Microelectromechanical Systems*, vol. 14, no. 4, pp. 857–863, Aug 2005.

[42] R. Zhang, J. Chu, H. Wang, and Z. Chen, "A multipurpose electrothermal microgripper for biological micro-manipulation," *Microsystem Technologies*, vol. 19, 01 2012.

[43] L. Yang, I. Paranawithana, K. Youcef-Toumi, and U. Tan, "Automatic vision-guided micromanipulation for versatile deployment and portable setup," *IEEE Transactions on Automation Science and Engineering*, vol. 15, no. 4, pp. 1609–1620, Oct 2018.

[44] L. Jiang and R. Cheung, "A review of silicon carbide development in mems applications," *Int. J. Computational Materials Science and Surface Engineering*, vol. 2, 01 2009.

[45] M. Savia and H. N. Koivo, "Contact micromanipulation: Survey of strategies," *IEEE/ASME Transactions on Mechatronics*, vol. 14, no. 4, pp. 504–514, Aug 2009.

[46] K. B. Yesin and B. J. Nelson, "A cad model based tracking system for visually guided microassembly," *Robotica*, vol. 23, no. 4, pp. 409–418, 2005.

[47] J. D. Wason, J. T. Wen, J. J. Gorman, and N. G. Dagalakis, "Automated multiprobe microassembly using vision feedback," *IEEE Transactions on Robotics*, vol. 28, no. 5, pp. 1090–1103, Oct 2012.

[48] A. Ferreira, C. Cassier, and S. Hirai, "Automatic microassembly system assisted by vision servoing and virtual reality," *IEEE/ASME Transactions on Mechatronics*, vol. 9, no. 2, pp. 321–333, June 2004.

[49] H. Xie and S. Régnier, "Three-dimensional automated micromanipulation using a nanotip gripper with multi-feedback," *Journal of Micromechanics and Microengineering*, vol. 19, no. 7, p. 075009, jun 2009.

[50] E. Avci, C. Nguyen, K. Ohara, M. Kojima, Y. Mae, and T. Arai, "Towards high-speed automated micromanipulation," in *2013 IEEE International Conference on Robotics and Automation*, May 2013, pp. 1718–1723.

[51] H. Xie, H. Zhang, J. Song, X. Meng, Y. Wen, and L. Sun, "High-precision automated micromanipulation and adhesive microbonding with cantilevered micropipette probes in the dynamic probing mode," *IEEE/ASME Transactions on Mechatronics*, vol. 23, no. 3, pp. 1425–1435, June 2018.

[52] M. Tortonese, H. Yamada, R. C. Barrett, and C. F. Quate, "Atomic force microscopy using a piezoresistive cantilever," in *TRANSDUCERS '91: 1991 International Conference on Solid-State Sensors and Actuators. Digest of Technical Papers*, June 1991, pp. 448–451.

[53] J. Jang, Y. Yoo, J. Kim, and J. Paik, "Sensor-based auto-focusing system using multi-scale feature extraction and phase correlation matching," *Sensors*, vol. 15, pp. 5747–5762, 03 2015.

[54] V. P. Namboodiri and S. Chaudhuri, "On defocus, diffusion and depth estimation," *Pattern Recognition Letters*, vol. 28, no. 3, pp. 311–319, Feb. 2007.

[55] S. Pertuz, D. Puig, and M. A. Garcia, "Analysis of focus measure operators for shape-from-focus," *Pattern Recognition*, vol. 46, no. 5, pp. 1415 – 1432, 2013.

[56] Y. Sun, S. Duthaler, and B. J. Nelson, "Autofocusing in computer microscopy: Selecting the optimal focus algorithm," *Microscopy Research and Technique*, vol. 65, no. 3, pp. 139–149, 2004.

[57] Yu Sun, S. Duthaler, and B. J. Nelson, "Autofocusing algorithm selection in computer microscopy," in *2005 IEEE/RSJ International Conference on Intelligent Robots and Systems*, Aug 2005, pp. 70–76.

[58] C. Batten, D. Holburn, B. Breton, and N. Caldwell, "Sharpness search algorithms for automatic focusing in the scanning electron microscope," *Scanning*, vol. 23, 01 2001.

[59] K. C. Lin, "Auto focusing under microscopic views," in *2007 IEEE Workshop on Signal Processing Systems*, Oct 2007, pp. 533–538.

[60] Q. Zhao, B. Liu, and Z. Xu, "Research and realization of an anti-noise auto-focusing algorithm," in *2013 5th International Conference on Intelligent Human-Machine Systems and Cybernetics*, vol. 2, Aug 2013, pp. 255–258.

[61] Seok Joo Lee, Kyunghwan Kim, Deok-Ho Kim, Jong-Oh Park, and Gwi Tae Park, "Recognizing and tracking of 3d-shaped micro parts using multiple visions for micromanipulation," in *MHS2001. Proceedings of 2001 International Symposium on Micromechatronics and Human Science (Cat. No.01TH8583)*, Sep. 2001, pp. 203–210.

[62] H. S. Parekh, D. G. Thakore, and U. K. Jaliya, "A survey on object detection and tracking methods," 2014.

[63] A. Samdurkar, S. Kamble, N. Thakur, and A. Patharkar, "Overview of object detection and tracking based on block matching techniques," 06 2017, pp. 313–319.

[64] Dongxiang Zhou and Hong Zhang, "Modified gmm background modeling and optical flow for detection of moving objects," in *2005 IEEE International Conference on Systems, Man and Cybernetics*, vol. 3, Oct 2005, pp. 2224–2229 Vol. 3.

[65] F. Mokhtarian, "Silhouette-based occluded object recognition through curvature scale space," *Machine Vision and Applications*, vol. 10, no. 3, pp. 87–97, Aug 1997.

[66] D. G. Lowe, "Distinctive image features from scale-invariant keypoints," *Int. J. Comput. Vision*, vol. 60, no. 2, pp. 91–110, Nov. 2004.

[67] H. Bay, A. Ess, T. Tuytelaars, and L. Van Gool, "Speeded-up robust features (surf)," *Comput. Vis. Image Underst.*, vol. 110, no. 3, pp. 346–359, Jun. 2008.

[68] . J. Athanesious and M. K. Suresh, "Implementation and comparison of kernel and silhouette based object tracking mr."

[69] K. Briechle and U. Hanebeck, "Template matching using fast normalized cross correlation," *Proceedings of SPIE - The International Society for Optical Engineering*, vol. 4387, 03 2001.

[70] H. O. Jacobs, H. F. Knapp, and A. Stemmer, "Practical aspects of kelvin probe force microscopy," *Review of Scientific Instruments*, vol. 70, no. 3, pp. 1756–1760, 1999.

[71] P. Gruetter, Y. Liu, P. LeBlanc, and U. Duerig, "Magnetic dissipation force microscopy," *Applied Physics Letters*, vol. 71, no. 2, pp. 279–281, 1997.

[72] J. Bausells, "Piezoresistive cantilevers for nanomechanical sensing," *Microelectronic Engineering*, vol. 145, pp. 9 – 20, 2015, micro/Nano Devices and Systems 2014 An open focused special thematic issue of Microelectronic Engineering.

[73] G. Schitter, K. J. Astrom, B. E. DeMartini, P. J. Thurner, K. L. Turner, and P. K. Hansma, "Design and modeling of a high-speed afm-scanner," *IEEE Transactions on Control Systems Technology*, vol. 15, no. 5, pp. 906–915, Sep. 2007.

[74] Sem image of piezoresistive cantilever. [Online]. Available: https://www.sclsensortech.com/portfolio-item/prsa-300x100%c2%b5m-si-tip-probes/

[75] W. Kuo, S. Chuang, C. Nian, and Y. Tarng, "Precision nano-alignment system using machine vision with motion controlled by piezoelectric motor," *Mechatronics*, vol. 18, no. 1, pp. 21 – 34, 2008.

[76] R. O. Duda and P. E. Hart, "Use of the hough transformation to detect lines and curves in pictures," *Commun. ACM*, vol. 15, no. 1, pp. 11–15, Jan. 1972.

# Appendix A - AFM Implementation

The evaluation of the positioning accuracy is done via an AFM scan. Section 4.4 already discusses the basic principle of it. A more detailed view on the actual implementation in SIMULINK is given here.
The following procedure is performed after the finished vision-guided alignment of the cantilever to the sample.

1. Move cantilever 2 $\mu$m up:
   In order to be able to compensate for deflections (up and down), the Z-piezo must be operated with a certain offset voltage. As the implemented piezo has a max. expansion of 8 $\mu m$, a setpoint of 2 $\mu m$ was chosen. This results from the vertical positioning accuracy of 1 $\mu m$ and the height of the structure of around 160 $nm$.

2. Apply voltage to Z-piezo till cantilever is in contact with the sample (gets deflected):
   Specifically, the Z-piezo's voltage is increased till the deflection signal corresponds to a tip-deflection of 500 $nm$.

3. Save deflection value of the cantilever and use it as a setpoint for the control loop:
   The control loop, shown in Figure A.1, adjusts the Z-piezo driving voltage to maintain the initial cantilever deflection throughout the measurement.

4. Start triangular trajectory scan of the XY-stage.

5. Record the Z-piezo driving voltage and the cantilever deflection signal during the scan. From them and the scanning trajectory the topography and error images are calculated.

6. Run algorithms to post-process recorded data and receive the AFM topography and error image. Run a plane fit algorithm to compensate for a possible sample tilt.

Figure A.1 shows the block diagram of the implemented AFM. With a 'Start AFM' command, the Z-Piezo is driven with a ramp till the cantilever is in contact with the sample. The deflection signal and the value of the ramp are then stored as setpoints. With the output of scan trajectories in x- and y-direction and simultaneous controlling

of the Z-Piezo voltage, the measurement is carried out. The recorded data is then processed in the 'Image acquisition / generation' block, which returns the results.

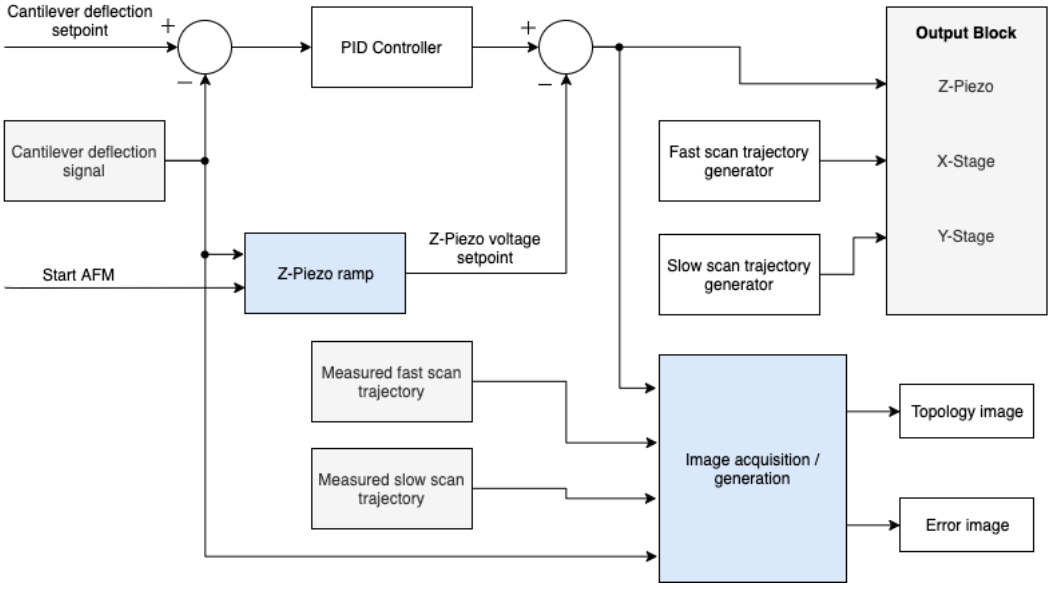


Figure A.1: Block diagram of the implemented AFM.

An example of a recorded topography and error image is shown in Figure A.2. Figure A.3 shows the implemented SIMULINK model of the AFM. The top/left part shows the control loop, consisting of the cantilever signal input, the PI controller and a sample-hold block to store the inital deflection value. In the top/right part the blocks to generate the scanning trajectory and the output block are implemented. The big block in the lower section of the figure is the image acquisition. Via the real scan trajectories (2 input blocks) and the output and input signals (Z-piezo voltage and cantilever deflection, respectively), the image is recorded while the scan is in progress.

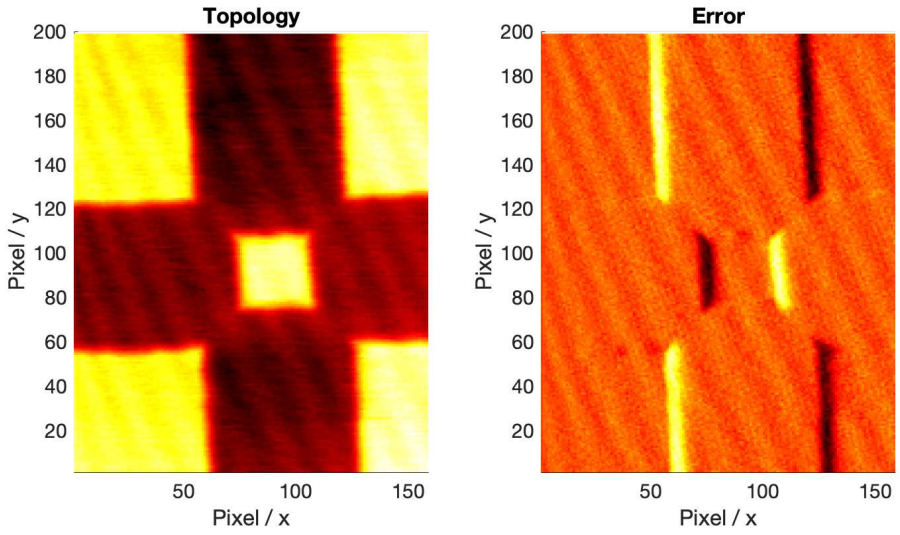


Figure A.2: Example of a recorded topography and error image.

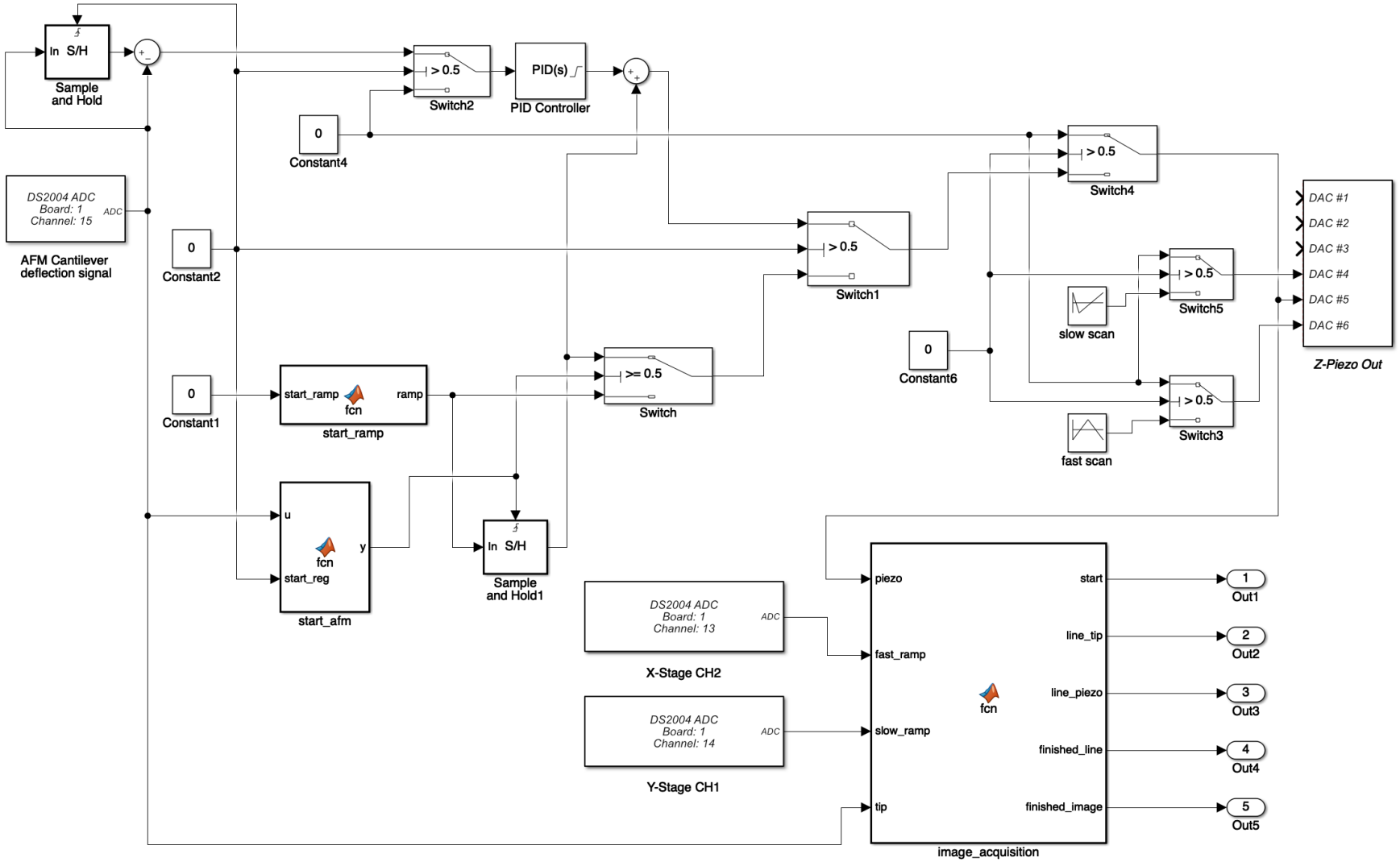


Figure A.3: SIMULINK model of the implemented AFM.

As the sample has an unintentional tilt and one wants to have a flat image of the investigated region, plane fitting is carried out. Figure A.4 shows an example of a recorded image (a,c) and the same plane fitted image (b,d).

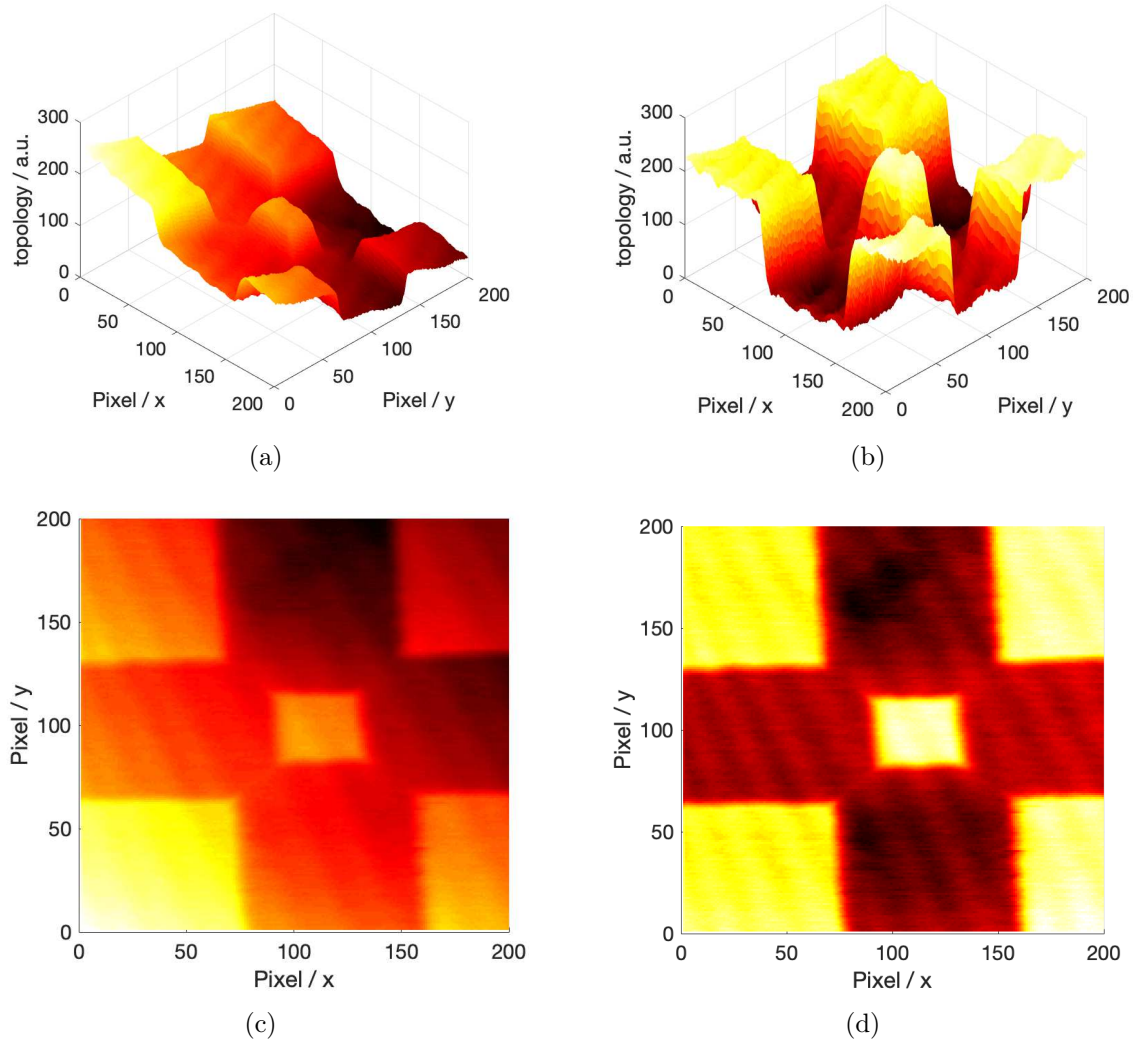


Figure A.4: Plane fitting of the AFM topography image / (a) and (c) depict the received AFM topography image / (b) and (d) show the plane fitted result.

With the recorded data in a N-by-3 matrix, a plane in the form of $z = a*x+b*y+c$ can be fitted. Each column of the matrix corresponds to the x, y and z values, denoted as X, Y and Z, respectively. The factors a, b and c are then calulated by: $a = \frac{X}{Z}$, $b = \frac{Y}{Z}$, $c = \frac{1}{Z}$. By evaluating the fitted plane $z$ at each point and subtracting it from the recorded data, a corrected image is obtained.

Hiermit erkläre ich, dass die vorliegende Arbeit gemäß dem Code of Conduct, insbesondere ohne unzulässige Hilfe Dritter und ohne Benutzung anderer als der angegebenen Hilfsmittel, angefertigt wurde. Die aus anderen Quellen direkt oder indirekt übernommenen Daten und Konzepte sind unter Angabe der Quelle gekennzeichnet.
Die Arbeit wurde bisher weder im In- noch im Ausland in gleicher oder in ähnlicher Form in anderen Prüfungsverfahren vorgelegt.

| | |
|---|---|
| Datum | Hackl Thomas |